**ERWIN STEIN AWARD '2001**
ICCES/Continental AG
Full-length paper
Hannover, Germany

# A FORMULATION FOR AN UNSATURATED POROUS MEDIUM UNDERGOING LARGE INELASTIC STRAINS

**Lorenzo Sanavia**
Department of Structural and Transportation Engineering
University of Padua, Italy
e–mail: sanavia@caronte.dic.unipd.it

**Key words:** Partially saturated porous media, large inelastic strains, finite elements

**Abstract.** *A formulation for a partially saturated porous medium undergoing large elastic or elastoplastic deformations is presented. The porous material is treated as a multiphase continuum with the pores of the solid skeleton filled by water and air, this last one at constant pressure. This pressure may either be the atmospheric pressure or the cavitation pressure. The governing equations at macroscopic level are derived in a spatial and a material setting. Solid grains and water are assumed to be incompressible at the microscopic level. The elasto-plastic behaviour of the solid skeleton is described by the multiplicative decomposition of the deformation gradient into an elastic and a plastic part. The effective stress state is limited by the Drucker-Prager yield surface. The water is assumed to obey Darcy's law. Numerical examples of the Liakopoulos' test and of strain localisation of dense and loose sand conclude the paper.*

## 1 Introduction

This paper presents a formulation for a saturated and partially saturated porous medium undergoing large elastic or elastoplastic strains. Mechanics of porous materials has a wide spectrum of engineering applications and hence, in recent years, several porous media models and their numerical solutions have appeared in the literature. Most of these models are restricted to fluid saturated materials and have been developed using small strain assumptions. For soils, large strains result when ultimate or serviceability limit state is reached, as for example during slope instability or during the consolidation process in compressible clays. In laboratory, this can be the case of drained or undrained biaxial tests of sands, where axial logarithmic strains of the order of 0.12-0.15 are reached [1, 2],

or the case of triaxial tests of peats, where axial strains of the order of 0.15 are measured. Among others, the phenomenon of strain localisation (i.e. strain accumulation in well defined narrow zones, also called shear bands) is most typical whereby large inelastic strains develop, at least inside the bands [1, 2, 3]. Moreover, it reveals also the strong coupling which occurs between the solid skeleton and the fluids filling the voids of the porous material.

More recently, porous media models have been extended to large strains, first in the framework of hypoelastoplasticity and, after the work of J.C. Simo for single-phase materials, also using hyperelastoplasticity. To the author knowledge, a partially saturated model has been put forward only in the framework of hypoelastoplasticity, based on an updated Lagrangian approach, Eulerian strain rate tensor and Jaumann stress rate [4]. In the present contribution, a partially saturated porous media model is developed in the framework of hyperelastoplasticity, extending the previous work of Sanavia et al. [5].

Conditions of partial saturation are of importance in engineering practice because many porous materials are in this natural state or can reach this state during deformations. Some simple examples can be found in soils or in concrete and in biological tissues, which can contain air or other gases in the pores together with liquids. For instance, this is the case of the soil zones above the free surface, or the case of deep reservoirs of hydrocarbon gas. The partially saturated state can also be reached during the deformation due, for instance, to earthquake in an earth dam or during the particular case of strain localisation of dense sands under globally undrained conditions, where negative water pressures are measured and cavitation of the pore water was observed [1, 2].

In the model developed in this paper, the porous medium is treated as an isothermal multiphase continuum with the pores of the solid skeleton filled by water and air, this last one at constant pressure (passive air phase assumption). This pressure may either be the atmospheric pressure or the cavitation pressure (isothermal monospecies approach). Quasi static loading conditions are considered. The governing equations at macroscopic level are derived in Section 3 in a spatial and a material setting and are based on averaging procedures (hybrid mixture theory). This model follows from the general Thermo-Hydro-Mechanical model developed in [6], which is briefly recalled in Section 2 for sake of completeness. Solid displacements and water pressures are the primary variables. The solid grains and water are assumed to be incompressible at microscopic level. The elasto-plastic behaviour of the solid skeleton is described by the multiplicative decomposition of the deformation gradient into an elastic and a plastic part, as described in Section 3.3. The modified effective stress in partially saturated conditions (Bishop like stress) in the form of Kirchhoff measure of the stress tensor and the logarithmic principal strains are used in conjunction with an hyperelastic free energy function. The effective stress state is limited by the Drucker-Prager yield surface and a particular "apex formulation" is presented in Section 6.1. Water is assumed to obey Darcy's law. In the partially saturated state, the water degree of saturation and the relative permeability are dependent on the capillary pressure by experimental functions. The spatial weak form of the governing equations, the temporal integration of the mixture mass balance equation, which is time dependent because of the seepage process of water, and the consistent linearisation are described in

Section 4, 5 and 6, respectively. In particular, the Generalised Trapezoidal Method is used for the time integration. Finally, the finite element discretisation in space is obtained by applying a Galerkin procedure in the spatial setting, using different shape functions for solid and water (see Section 7).
Numerical examples of this research in progress on large elastic or inelastic strains in saturated and partially saturated porous media highlight the developments in Section 8. The first one is the simulation of the experimental Liakopoulos' test, for which the measured experimental desaturation of the column from the top to the bottom surface is well described. In the second example, a stability problem on loose or dense sand is studied. The equivalent plastic strain distribution shows the presence of a localised zone (Drucker-Prager model is used, with non associated flow rule), with negative water pressures induced by the dilatancy of the dense sand below the cavitation pressure at ambient temperature (of -96 kPa) inside the shear band. For the aspects of the regularization properties of the multiphase model at localisation, due to the presence of a Laplacian in the mass balance equation of the fluids, the interesting reader can see [7] and [8].
As notation and symbols are concerned, bold-face letters denote tensors; capital or lower case letters are used for tensors in the reference or in actual configuration. The symbol '$\cdot$' denotes a single contraction of (adjacent) indices of two tensors (e.g. $\boldsymbol{a} \cdot \boldsymbol{b} = a_i b_i, \boldsymbol{c} \cdot \boldsymbol{d} = c_{ij} d_{jk}$), while the symbol ':' denotes a double contraction of (adjacent) indices of two tensors of rank two or/and higher (e.g. $\boldsymbol{c} : \boldsymbol{d} = c_{ij} d_{ij}, \boldsymbol{e} : \boldsymbol{f} = e_{ijkl} f_{kl}$). Cartesian co-ordinates are used throughout.

## 2 General Mathematical Model of Thermo-Hydro-Mechanical Transient Behaviour of Geomaterials

The full mathematical model necessary to simulate thermo-hydro-mechanical transient behaviour of fully and partially saturated porous media is developed in [6] using averaging theories following Hassanizadeh and Gray [9, 10]. The underlying physical model, thermodynamic relations and constitutive equations for the constituents, as well as governing equations are briefly summarised for sake of completeness in the present section. The governing equations of the simplified model used in the finite element discretisation are described in Section 3.
The partially saturated porous medium is treated as multiphase system composed of $\pi = 1, \cdots, k$ constituents with the voids of the solid skeleton ($s$) filled with water ($w$) and gas ($g$). The latter is assumed to behave as an ideal mixture of two species: dry air (noncondensable gas, $ga$) and water vapour (condensable one, $gw$). Using spatial averaging operators defined over a representative elementary volume R.E.V. (of volume $dv(\boldsymbol{x}, t)$ in the deformed configuration, $B_t$, see Figure 1, where $\boldsymbol{x}$ is the vector of the spatial co-ordinates and $t$ is the current time), the microscopic equations are integrated over the R.E.V. giving the macroscopic balance equations. At the macroscopic level the porous media material is hence modelled by a substitute continuum of volume $B_t$ with boundary $\partial B_t$ that fills the entire domain simultaneously, instead of the real fluids and the solid

which fill only a part of it. In these substitute continuum each constituent $\pi$ has a reduced density which is obtained through the volume fraction $\eta^\pi(\boldsymbol{x},t) = dv^\pi(\boldsymbol{x},t)/dv(\boldsymbol{x},t)$ with the constraint

$$\sum_{\pi=1}^{k} \eta^\pi = 1 \tag{1}$$

where $dv^\pi(\boldsymbol{x},t)$ is the $\pi$-phase volume inside the R.E.V. in the actual placement $\boldsymbol{x}$.

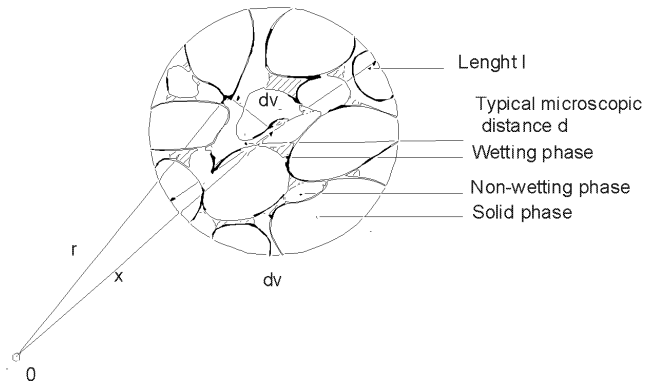


Figure 1: Typical averaging volume $dv(\boldsymbol{x},t)$ of a porous medium consisting of three constituents [6].

In this formulation heat conduction, vapour diffusion, heat convection, water flow due to pressure gradients or capillary effects and latent heat transfer due to water phase change (evaporation and condensation) inside the pores are taken into account. The solid is deformable and non-polar, and the fluid, the solid and the thermal fields are coupled. All fluids are in contact with the solid phase. The constituents are assumed to be isotropic, homogeneous, immiscible except for dry air and vapour, and chemically non reacting. Local thermal equilibrium between solid matrix, gas and liquid phases is assumed, so that the temperature is the same for all the constituents. The state of the medium is described by water pressure $p^w$, gas pressure $p^g$, temperature $\theta$ and displacement vector of the solid matrix $\boldsymbol{u}$.
Before summarising the macroscopic balance equations, we specify the kinematics introducing the notion of initial and current configuration (Figure 2). In the following, the stress is defined as tension positive for the solid phase, while pore pressure is defined as compressive positive for the fluids.

### 2.1 Kinematic Equations

At the macroscopic level the multiphase medium is described as the superposition of all $\pi$-phases, whose material points $X^\pi$ with coordinates $\boldsymbol{X}^\pi$ in the reference configuration $B_0^\pi$ at time $t = t_0$ can occupy simultaneously each spatial point $\boldsymbol{x}$ in the deformed configuration $B_t$ at time $t$. In the Lagrangian description of the motion in terms of material coordinates

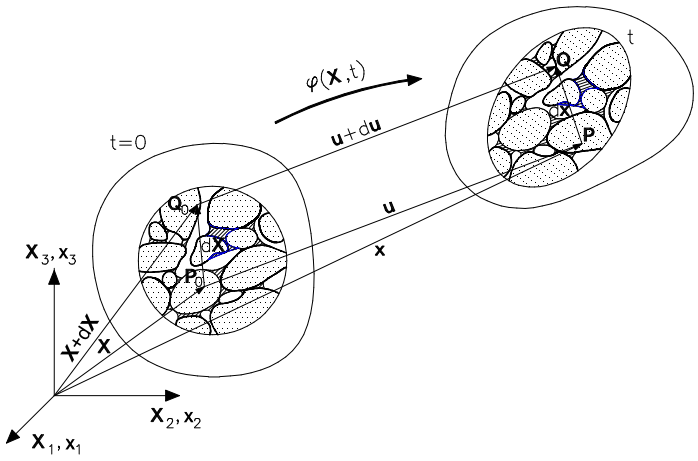


Figure 2: Initial and current configuration of a multiphase medium.

the position of each material point in the actual configuration $\boldsymbol{x}$ is a function of its placement $\boldsymbol{X}^\pi$ in a chosen reference configuration $B_0^\pi$ and of the current time $t$,

$$\boldsymbol{x} = \boldsymbol{\chi}^\pi(\boldsymbol{X}^\pi, t) \tag{2}$$

with $\boldsymbol{x} = \boldsymbol{x}^\pi$ or it is given by the sum of the reference position $\boldsymbol{X}^\pi$ and the displacement $\boldsymbol{u}^\pi = (\boldsymbol{X}^\pi, t)$ at time $t$

$$\boldsymbol{x} = \boldsymbol{X}^\pi + \boldsymbol{u}^\pi(\boldsymbol{X}^\pi, t) \tag{3}$$

In eq. (2), $\boldsymbol{\chi}^\pi(\boldsymbol{X}^\pi, t)$ is a continuous and bijective motion function (deformation map) of each phase because the jacobian $J^\pi$ of the each motion function

$$J^\pi = \det \frac{\partial \boldsymbol{\chi}^\pi(\boldsymbol{X}^\pi, t)}{\partial \boldsymbol{X}^\pi} > 0 \tag{4}$$

is restricted to be a positive value. The deformation gradient $\boldsymbol{F}^\pi(\boldsymbol{X}^\pi, t)$ is defined as

$$\boldsymbol{F}^\pi = \operatorname{Grad}^\pi \boldsymbol{\chi}^\pi(\boldsymbol{X}^\pi, t) \tag{5}$$

where the differential operator $\operatorname{Grad}^\pi$ denotes partial differentiation with respect to the reference position $\boldsymbol{X}^\pi$. Hence, from eq. (4), $J^\pi = \det \boldsymbol{F}^\pi$.
The velocity and the acceleration of each constituent are given as

$$\boldsymbol{V}^\pi = \frac{\partial \boldsymbol{\chi}^\pi(\boldsymbol{X}^\pi, t)}{\partial t} \qquad \boldsymbol{A}^\pi = \frac{\partial^2 \boldsymbol{\chi}^\pi(\boldsymbol{X}^\pi, t)}{\partial t^2} \tag{6}$$

Due to the non singularity of the Lagrangian relationship (2), the existence of its inverse function leads to the description of the motion in terms of spatial coordinates,

$$\boldsymbol{X}^\pi = [\boldsymbol{\chi}^\pi]^{-1}(\boldsymbol{x}, t) \tag{7}$$

The inverse $[\boldsymbol{F}^\pi]^{-1}(\boldsymbol{x},t)$ of the deformation gradient is given by

$$[\boldsymbol{F}^\pi]^{-1} = \text{grad}\boldsymbol{X}^\pi(\boldsymbol{x},t) \tag{8}$$

where the differential operator 'grad' is now referred to spatial coordinates $\boldsymbol{x}$. The spatial parametrization of the velocity is given by

$$\boldsymbol{v}^\pi = \boldsymbol{v}^\pi(\boldsymbol{x},t) = \boldsymbol{V}^\pi \circ [\boldsymbol{\chi}^\pi]^{-1} \tag{9}$$

where '$\circ$' denotes the composition of functions. The parametrization of the spatial acceleration is related to the spatial velocity by the application of the chain rule to (9)

$$\boldsymbol{a}^\pi = \boldsymbol{a}^\pi(\boldsymbol{x},t) = \frac{\partial \boldsymbol{v}^\pi}{\partial t} + \text{grad}\boldsymbol{v}^\pi \cdot \boldsymbol{v}^\pi = \boldsymbol{A}^\pi \circ [\boldsymbol{\chi}^\pi]^{-1} \tag{10}$$

Since the individual constituents follow in general different motions, different material time derivatives must be formulated. For an arbitrary scalar-valued function $f^\pi(\boldsymbol{x},t)$ its material time derivative following the velocity of the constituents $\pi$ is defined by [6]

$$\frac{D^\pi f^\pi}{Dt} = \frac{\partial f^\pi}{\partial t} + \text{grad}f^\pi \cdot \boldsymbol{v}^\pi \tag{11}$$

where $f^\pi(\boldsymbol{x},t)$ must be substituted by $\boldsymbol{f}^\pi(\boldsymbol{x},t)$ in case of vector or tensor valued function $\boldsymbol{f}^\pi(\boldsymbol{x},t)$. Thus $\boldsymbol{a}^\pi = D^\pi \boldsymbol{v}^\pi / Dt$.

In multiphase materials theory it is common to assume the motion of the solid as a reference and to describe the fluids in terms of motion relative to the solid. This means that a fluid relative velocity and the material time derivative with respect to the solid are introduced. The solid motion can be described both in terms of material or spatial coordinates. The second approach is now presented because the most natural numerical formulation of the elasto-plastic initial boundary value problem is based on the weak form of the balance equations in a spatial setting.
The fluid relative velocity $\boldsymbol{v}^{\pi s}(\boldsymbol{x},t)$ in spatial parametrization or diffusion velocity is given by

$$\boldsymbol{v}^{\pi s}(\boldsymbol{x},t) = \boldsymbol{v}^\pi(\boldsymbol{x},t) - \boldsymbol{v}^s(\boldsymbol{x},t) \tag{12}$$

and the material time derivative of $f^\pi(\boldsymbol{x},t)$ with respect to the moving solid phase $(s)$ is given by

$$\frac{D^s f^\pi}{Dt} = \frac{D^\pi f^\pi}{Dt} + \text{grad}f^\pi \cdot \boldsymbol{v}^{s\pi} \quad \text{with} \quad \boldsymbol{v}^{s\pi} = -\boldsymbol{v}^{\pi s} \tag{13}$$

For the section closure, the material and the spatial velocity gradient of the solid will be recalled. The first one is given as

$$\boldsymbol{L}^s = \text{Grad}^s \boldsymbol{V}^s = \frac{\partial \boldsymbol{F}^s}{\partial t} = \boldsymbol{D}^s + \boldsymbol{W}^s \tag{14}$$

where $\boldsymbol{D}^s(\boldsymbol{X}^s,t)$ and $\boldsymbol{W}^s(\boldsymbol{X}^s,t)$ are the symmetric and the skew-symmetric part of $\boldsymbol{L}^s(\boldsymbol{X}^s,t)$, while the spatial velocity gradient $\boldsymbol{l}^s(\boldsymbol{x},t)$ is defined as the gradient of the velocity (9) respect to the spatial coordinates, i.e.

$$\boldsymbol{l}^s = \text{grad}\boldsymbol{v}^s = \frac{\partial \boldsymbol{F}^s}{\partial t}\cdot[\boldsymbol{F}^s]^{-1} = \boldsymbol{d}^s + \boldsymbol{w}^s \tag{15}$$

where $\boldsymbol{d}^s(\boldsymbol{x},t)$ and $\boldsymbol{w}^s(\boldsymbol{x},t)$ are the symmetric and the skew-symmetric part of $\boldsymbol{l}^s(\boldsymbol{x},t)$, also called spatial rate of deformation tensor and spin tensor, respectively.
All strain measures and strain rates for each constituent follow similarly to classical non-linear continuum mechanics, but are not reported here because they are not useful for the approach developed in the sequel.

### 2.2 Mass Balance Equations

The averaged macroscopic balance equation for the solid phase is

$$\frac{D^s\rho_s}{Dt} + \rho_s\,\text{div}\boldsymbol{v}^s = \frac{\partial\rho_s}{\partial t} + \text{div}(\rho_s\boldsymbol{v}^s) = 0 \tag{16}$$

where $\boldsymbol{v}^s(\boldsymbol{x},t)$ is the mass averaged solid velocity, $\rho_s(\boldsymbol{x},t)$ is the averaged density of the solid related to the intrinsic averaged density $\rho^s(\boldsymbol{x},t)$ by the volume fraction $\eta^s(\boldsymbol{x},t)$.
For the generic $\pi$-phase the relationship between the averaged density and the intrinsic averaged density is

$$\rho_\pi(\boldsymbol{x},t) = \eta^\pi(\boldsymbol{x},t)\rho^\pi(\boldsymbol{x},t) \tag{17}$$

where the intrinsic density $\rho^\pi(\boldsymbol{x},t)$ is also named real or true density in the so called Theory of Porous Media, e.g. [11].
The mass balance equation for water is

$$\frac{D^w\rho_w}{Dt} + \rho_w\,\text{div}\boldsymbol{v}^w = \frac{\partial}{\partial t}(nS_w\rho^w) + \text{div}(nS_w\rho^w\boldsymbol{v}^w) = \rho_w e^w \tag{18}$$

where $\rho_w e^w(\boldsymbol{x},t)$ is the quantity of water per unit time and volume lost through evaporation. The corresponding equations for dry air and vapour are respectively

$$\frac{D^{ga}\rho_{ga}}{Dt} + \rho_{ga}\,\text{div}\boldsymbol{v}^{ga} = \frac{\partial}{\partial t}(nS_g\rho^{ga}) + \text{div}(nS_g\rho^{ga}\boldsymbol{v}^{ga}) = 0 \tag{19}$$

$$\frac{D^{gw}\rho_{gw}}{Dt} + \rho_{gw}\,\text{div}\boldsymbol{v}^{gw} = \frac{\partial}{\partial t}(nS_g\rho^{gw}) + \text{div}(nS_g\rho^{gw}\boldsymbol{v}^{gw}) = \rho_{gw}e^{gw} \tag{20}$$

where $n(\boldsymbol{x},t)$ is the porosity of the medium defined as

$$n = \frac{dv^w + dv^g}{dv} = \frac{dv^{voids}}{dv} = 1 - \eta^s \tag{21}$$

and $S_w$ and $S_g$ the water and gas degree of saturation. The following relationships hold

$$\begin{aligned} \eta^w &= nS_w \text{ with } S_w = \frac{dv^w}{dv^w + dv^g} \\ \eta^g &= nS_g \text{ with } S_g = \frac{dv^g}{dv^w + dv^g} \end{aligned} \tag{22}$$

with the saturation constraint $S_w + S_g = 1$.

### 2.3 Linear Momentum Balance Equations

The linear momentum balance equation for the solid and the $\pi$-fluid are

$$\mathrm{div}\boldsymbol{t}^s + \rho_s[\boldsymbol{g} - \boldsymbol{a}^s] + \rho_s\hat{\boldsymbol{t}}^s = \boldsymbol{0} \tag{23}$$

and

$$\mathrm{div}\boldsymbol{t}^\pi + \rho_\pi[\boldsymbol{g} - \boldsymbol{a}^\pi] + \rho_\pi[\boldsymbol{e}^\pi + \hat{\boldsymbol{t}}^\pi] = \boldsymbol{0} \tag{24}$$

respectively, where $\boldsymbol{t}^\pi(\boldsymbol{x}, t)$ is the partial Cauchy stress tensor defined via the constitutive equation presented in Section 2.6. $\hat{\boldsymbol{t}}^\pi(\boldsymbol{x}, t)$ accounts for the exchange of momentum due to mechanical interaction with other phases, $\rho_\pi\boldsymbol{a}^\pi$ the volume density of the inertial force, $\rho_\pi\boldsymbol{g}$ the volume density of gravitational force and $\boldsymbol{e}^\pi(\boldsymbol{x}, t)$ takes into account the momentum exchange due to averaged mass supply or mass exchange between the fluid and the gas phases and the change of density. The linear momentum balance equation of the multiphase medium is subjected to the constraint [6]

$$\sum_{\pi=1}^{k} \rho_\pi[\boldsymbol{e}^\pi + \hat{\boldsymbol{t}}^\pi] = \boldsymbol{0} \tag{25}$$

### 2.4 Angular Momentum Balance Equation

All the phases are considered microscopically non-polar and hence at macroscopic level the angular momentum balance equation states that the partial stress tensor is symmetric [6]

$$\boldsymbol{t}^\pi = [\boldsymbol{t}^\pi]^T \tag{26}$$

### 2.5 Energy Balance Equation and Entropy Inequality

These two relationships are simply quoted from [6]; the second one is useful for the development of the constitutive equations.
The energy balance equation for the $\pi$-phase may be written as

$$\rho_\pi \frac{D^\pi E^\pi}{Dt} = \boldsymbol{t}^\pi : \boldsymbol{d}^\pi + \rho_\pi h^\pi - \mathrm{div}\boldsymbol{q}^\pi + \rho_\pi R^\pi \tag{27}$$

where $\rho_\pi R^\pi$ represents the exchange of energy between the $\pi$-phase and other phases of the medium due to phase change and mechanical interaction, $\boldsymbol{q}^\pi$ is the internal heat flux, $h^\pi$ results from the heat sources and $\boldsymbol{d}^\pi$ is the spatial rate of the deformation tensor. $E^\pi$ accounts for the specific internal energy of the volume element.

The entropy inequality for the mixture is

$$\sum_\pi \left[ \rho_\pi \frac{D^\pi \lambda^\pi}{Dt} + \rho_\pi e^\pi \lambda^\pi + \mathrm{div}\frac{\boldsymbol{q}^\pi}{\theta^\pi} - \frac{\rho_\pi h^\pi}{\theta^\pi} \right] \geq 0 \tag{28}$$

where $\theta^\pi$ is the absolute temperature, $\lambda^\pi$ is the specific entropy of the constituent $\pi$ and $e^\pi\lambda^\pi$ the entropy supply due to mass exchange.

### 2.6 Constitutive Equations

The momentum exchange term $\rho_\pi \hat{\boldsymbol{t}}^\pi$ of the linear momentum balance equation of the fluid can be expressed as [6]

$$\rho_\pi \hat{\boldsymbol{t}}^\pi = -\mu^\pi {\eta^\pi}^2 \boldsymbol{k}^{-1} \cdot \boldsymbol{v}^{\pi s} + p^\pi \,\mathrm{grad}\eta^\pi \qquad \text{with} \qquad \pi = g, w \tag{29}$$

Here $\boldsymbol{k} = k^{r\pi}\boldsymbol{k}^\pi$, where $\boldsymbol{k}^\pi(\boldsymbol{x}, t) = \boldsymbol{k}^\pi(\rho^\pi, \eta^\pi, T)$ is the intrinsic permeability tensor of dimension $[L^2]$ depending in the isotropic case on the porosity of the medium, $k^{r\pi}(S_\pi)$ is the relative permeability parameter and $\mu^\pi$ is the dynamic viscosity. The relative permeability is function of the $\pi$-phase degree of saturation $S_\pi$ and is determined in laboratory tests (see e.g. [6]).

The partial stress tensor in the fluid phase of linear momentum balance equation (24) is related to the macroscopic pressure $p^\pi(\boldsymbol{x}, t)$ of the $\pi$ phase

$$\boldsymbol{t}^\pi = -\eta^\pi p^\pi \mathbf{1} \tag{30}$$

where $\mathbf{1}$ is the second order unit tensor.

From the entropy inequality it can be also shown that the spatial solid stress tensor $\boldsymbol{t}^s(\boldsymbol{x}, t)$ of the linear momentum balance equation (23) is decomposed as follows

$$\boldsymbol{t}^s = \eta^s[\boldsymbol{t}_e^s - p^s \mathbf{1}] \tag{31}$$

and that the effective Cauchy stress tensor $\boldsymbol{\sigma}'(\boldsymbol{x}, t)$, which is responsible for all major deformation in the solid skeleton, is

$$\boldsymbol{\sigma}' = \eta^s \boldsymbol{t}_e^s \tag{32}$$

In eq. (31), $\boldsymbol{t}_e^s(\boldsymbol{x}, t)$ is the dissipative part [12] or effective stress tensor of the solid phase, while $p^s(\boldsymbol{x}, t)$ is the equilibrium part, also called solid pressure, with $p^s = S_w p^w + S_g p^g$. From the previous equations, it follows that the total Cauchy stress tensor $\boldsymbol{\sigma} = \boldsymbol{t}^s + \boldsymbol{t}^w + \boldsymbol{t}^g$ can be written in the usual form used in soil mechanics

$$\boldsymbol{\sigma} = \boldsymbol{\sigma}' - [S_w p^w + S_g p^g]\mathbf{1} \tag{33}$$

The constitutive law for the solid skeleton used in this paper will be discussed in Section 3.

The pressure $p^g(\boldsymbol{x}, t)$ is given in the sequel. For gaseous mixture of dry air and water vapour the ideal gas law is introduced because the moist air is assumed to be a perfect mixture of two ideal gases. The equation of state of perfect gas (the Clapeyron equation) and Dalton's law applied to dry air ($ga$), water vapour ($gw$) and moist air ($g$), yield

$$p^{ga} = \rho^{ga} R\theta / M_a \qquad p^{gw} = \rho^{gw} R\theta / M_w \tag{34}$$

$$p^g = p^{ga} + p^{gw} \qquad \rho^g = \rho^{ga} + \rho^{gw} \tag{35}$$

In the partially saturated zones water is separated from its vapour by a concave meniscus (capillary water). Due to the curvature of this meniscus the sorption equilibrium equation gives the relationship between the capillary pressure $p^c(\boldsymbol{x},t)$ and the gas $p^g(\boldsymbol{x},t)$ and water pressure $p^w(\boldsymbol{x},t)$ [12]

$$p^c = p^g - p^w \tag{36}$$

The equilibrium water vapour pressure $p^{gw}(\boldsymbol{x},t)$ can be obtained from the Kelvin-Laplace equation

$$p^{gw} = p^{gws}(\theta)\exp\left(\frac{p^c M_w}{\rho^w R\theta}\right) \tag{37}$$

where the water vapour saturation pressure $p^{gws}$, depending only upon temperature $\theta(\boldsymbol{x},t)$, can be calculated from the Clausius-Clapeyron equation or from empirical correlation.

The saturation $S_\pi(\boldsymbol{x},t)$ is an experimentally determined function of capillary pressure $p^c$ and temperature $\theta$

$$S_\pi = S_\pi(p^c,\theta) \tag{38}$$

For the binary gas mixture of the dry air and water vapour, Fick's law gives the following relative velocities $\boldsymbol{v}_g^\pi = \boldsymbol{v}^\pi - \boldsymbol{v}^g$, $(\pi = ga, gw)$, of the diffusing species

$$\boldsymbol{v}_g^{ga} = -\frac{M_a M_w}{M_g^2}\boldsymbol{D}_g \cdot \operatorname{grad}\left(\frac{p^{ga}}{p^g}\right) = -\boldsymbol{v}_g^{gw} \tag{39}$$

where $\boldsymbol{D}_g$ is the effective diffusivity tensor and $M_g$ is the molar mass of the gas mixture

$$\frac{1}{M_g} = \frac{\rho^{gw}}{\rho^g}\frac{1}{M_w} + \frac{\rho^{ga}}{\rho^g}\frac{1}{M_a}. \tag{40}$$

### 2.7 Initial and Boundary Conditions

For model closure it is necessary to define the initial and boundary conditions. The initial conditions specify the full fields of gas pressure, water pressure, temperature, displacements and velocity

$$\begin{gathered} p^g = p_0^g, \quad p^w = p_0^w, \quad \theta = \theta_0, \\ \boldsymbol{u} = \boldsymbol{u}_0, \quad \dot{\boldsymbol{u}} = \dot{\boldsymbol{u}}_0, \quad \text{at} \quad t = t_0. \end{gathered} \tag{41}$$

The boundary conditions can be imposed values on $\partial B_\pi$ or fluxes on $\partial B_\pi^q$ , where the boundary is $\partial B = \partial B_\pi \cup \partial B_\pi^q$ . The imposed values on the boundary for gas pressure, water pressure, temperature and displacements are as follows:

$$\begin{gathered} p^g = \hat{p}^g \quad \text{on} \quad \partial B_g, \quad p^w = \hat{p}^w \quad \text{on} \quad \partial B_w, \\ \theta = \hat{\theta} \quad \text{on} \quad \partial B_\theta, \quad \boldsymbol{u} = \hat{\boldsymbol{u}} \quad \text{on} \quad \partial B_u \quad \text{for} \quad t \geq t_0. \end{gathered} \tag{42}$$

The volume average flux boundary conditions for dry air water and species conservation equations and the energy equation to be imposed at the interface between the porous media and the surrounding fluid (the natural boundary conditions) are the following:

$$
\begin{aligned}
[\rho^{ga}\boldsymbol{v}^{g} - \rho^{g}\boldsymbol{v}_{g}^{gw}] \cdot \boldsymbol{n} &= q^{ga} \quad \text{on} \quad \partial B_{g}^{q} \\
[\rho^{gw}\boldsymbol{v}^{g} + \rho^{w}\boldsymbol{v}^{w} + \rho^{g}\boldsymbol{v}_{g}^{gw}] \cdot \boldsymbol{n} &= \beta_{c}[\rho^{gw} - \rho_{\infty}^{gw}] + q^{gw} + q^{w} \quad \text{on} \quad \partial B_{c}^{q} \\
-[\rho^{w}\boldsymbol{v}^{w}\Delta h_{vap} - \lambda_{eff}\nabla\theta] \cdot \boldsymbol{n} &= \alpha_{c}[\theta - \theta_{\infty}] + q^{\theta} \quad \text{on} \quad \partial B_{\theta}^{q}
\end{aligned}
\tag{43}
$$

for $t \geq t_0$, where $\boldsymbol{n}(\boldsymbol{x}, t)$ is the vector perpendicular to the surface of the porous medium, pointing toward the surrounding gas, $\rho_{\infty}^{gw}(\boldsymbol{x}, t)$ and $\theta_{\infty}(\boldsymbol{x}, t)$ are, respectively, the mass concentration of water vapour and temperature in the undisturbed gas phase distant from the interface, $\alpha_c(\boldsymbol{x}, t)$ and $\beta_c(\boldsymbol{x}, t)$ are convective heat and mass transfer coefficients, while $q^{ga}(\boldsymbol{x}, t)$, $q^{gw}(\boldsymbol{x}, t)$, $q^{w}(\boldsymbol{x}, t)$ and $q^{\theta}(\boldsymbol{x}, t)$ are the imposed dry air flux, imposed vapour flux, imposed liquid flux and imposed heat flux, respectively.
The traction boundary conditions for the displacement field related to the total Cauchy stress tensor $\boldsymbol{\sigma}(\boldsymbol{x}, t)$ are

$$
\boldsymbol{\sigma} \cdot \boldsymbol{n} = \bar{\boldsymbol{t}} \text{ on } \partial B_{u}^{q} \tag{44}
$$

where $\bar{\boldsymbol{t}}(\boldsymbol{x}, t)$ is the imposed Cauchy traction vector.

## 3 Macroscopic Balance Equations for an Isothermal Saturated and Partially Saturated Medium

In this section the macroscopic balance equations for mass and linear momentum of a simplified model that we shall use in the sequel are obtained. The constitutive equations for finite elastoplasticity as well as their algorithmic counterpart will close the present section.
The following assumptions are now introduced in the general model previously presented:

- all the processes are isothermal. This means that the energy balance equation, eq. (27) is no more necessary;
- at the micro level, the porous medium is assumed to be constituted of incompressible solid and water constituents, while gas is considered compressible. The averaged intrinsic density $\rho^{\pi}(\boldsymbol{x}, t)$, $\pi = s, w$, is hence constant, while the averaged density $\rho_{\pi}(\boldsymbol{x}, t)$ can vary due to the volume fraction $\eta^{\pi}(\boldsymbol{x}, t)$. Consequently, the density of the mixture $\rho(\boldsymbol{x}, t)$, eq. (60) and the porosity $n(\boldsymbol{x}, t)$ can change during the deformation of the porous medium;
- phase change between the fluid phases is neglected;
- the process is considered as quasi-static, so the solid and fluids accelerations are neglected;

- the passive air phase assumption will be introduced during the development of the mathematical model.

The formulation in terms of spatial coordinates is now presented.

### 3.1 Mass Balance Equation

Taking into account the incompressibility constraint of the solid and water constituents in (16) and (18), the mass balance equation for the solid and water phase become

$$\frac{\partial}{\partial t}[1-n] + \operatorname{div}([1-n]\boldsymbol{v}^s) = 0 \tag{45}$$

$$\frac{\partial n S_w}{\partial t} + \operatorname{div}(n S_w \boldsymbol{v}^w) = 0 \tag{46}$$

where the definition of the phase averaged density (17) has been introduced, thus eliminating the intrinsic (constant) averaged density $\rho^\pi(\boldsymbol{x},t)$ ($\pi = s, w$). Using the concept of material time derivative (11), eq. (45) is rewritten as

$$\frac{D^s}{Dt}[1-n] + [1-n]\operatorname{div}\boldsymbol{v}^s = 0 \tag{47}$$

where the classical relationship

$$\operatorname{div}\boldsymbol{v}^s = \frac{D^s J^s}{Dt}[J^s]^{-1} \tag{48}$$

can be introduced [14] for the solid deformation. The time integration of (47) gives the evolution law for the porosity $n(\boldsymbol{x},t)$ related to the determinant $J^s(\boldsymbol{X}^s,t)$ of the deformation gradient $\boldsymbol{F}^s(\boldsymbol{X}^s,t)$

$$n = 1 - [1-n_0][J^s]^{-1} \tag{49}$$

where $n_0(\boldsymbol{X}^s)$ is the porosity in the reference configuration at $t = t_0$ (or initial porosity). Because of the relation $\eta^s(\boldsymbol{x},t) = 1 - n(\boldsymbol{x},t)$, eq. (49) can be rewritten as

$$\eta^s = \eta^s_0[J^s]^{-1} \tag{50}$$

where $\eta^s_0(\boldsymbol{X}^s)$ is the solid volume fraction in the reference configuration at $t = t_0$.

The gas mass balance equation

$$\frac{\partial}{\partial t}(n S_g \rho^g) + \operatorname{div}(n S_g \rho^g \boldsymbol{v}^g) = 0 \tag{51}$$

is obtained by summation of the corresponding equations for the dry air and the water vapour and taking into account the Dalton's law (35) and introducing the mass averaged gas velocity $\boldsymbol{v}^g = [\rho^{ga}\boldsymbol{v}^{ga} + \rho^{gw}\boldsymbol{v}^{gw}]/\rho^g$.

The sum of the mass balance equation of the three constituents (45), (46) and (51) produces the following mass balance equation for the mixture under consideration

$$\mathrm{div}([1-n]\boldsymbol{v}^s + nS_w\boldsymbol{v}^w + nS_g\boldsymbol{v}^g) = 0 \tag{52}$$

in which the passive air phase assumption

$$p^g \cong \text{const.} \tag{53}$$

has been introduced, thus eliminating the terms of (51) depending from the spatial or the time variation of $\rho^g$. This pressure may either be the atmospheric pressure or the cavitation pressure at a certain temperature (e.g. the ambient temperature). The first case is a common assumption in soil mechanics because in many cases occurring in practice the air pressure is close to the atmospheric pressure as the pores are interconnected [13]. The second case derives from the experimental observations [1] and the obtained model is also called *Isothermal Monospecies Approach*, which can be used to simulate cavitation at localisation in initially water saturated dense sands under globally undrained conditions, as first developed in [7] for the geometrically linear case. In fact, in this situation, neglecting air dissolved in water, only two fluid phases are present after cavitation: liquid water and water vapour at cavitation pressure, which can be neglected.

Introducing the water and the gas velocity relative to the solid, i.e. $\boldsymbol{v}^{ws} = \boldsymbol{v}^w - \boldsymbol{v}^s$ and $\boldsymbol{v}^{gs} = \boldsymbol{v}^g - \boldsymbol{v}^s$, the mixture mass balance equation (52) becomes

$$\mathrm{div}(\boldsymbol{v}^s + nS_w\boldsymbol{v}^{ws} + nS_g\boldsymbol{v}^{gs}) = 0 \tag{54}$$

The terms $nS_w\boldsymbol{v}^{ws}(\boldsymbol{x},t)$ and $nS_g\boldsymbol{v}^{gs}(\boldsymbol{x},t)$ represent the filtration water and gas velocity, respectively. The fluid velocity relative to the solid is related to the fluid pressure by the linear momentum balance equation for fluid phase after the introduction of the constitutive law (29), which gives the Darcy's law (63), as will be demonstrated in the sequel. Taking into account the expression of the Darcy's law for the gas, than the passive air phase assumption implies that $\boldsymbol{v}^{gs}$ is negligible and hence the mass balance equation for the mixture (54) becomes

$$\mathrm{div}(\boldsymbol{v}^s + nS_w\boldsymbol{v}^{ws}) = 0 \tag{55}$$

In case of fully saturated conditions, $S_w = 1$ and hence the previous equation is reduced to the one of the saturated model.

### 3.2 Linear Momentum Balance Equation

Neglecting the inertial term in (23) and (24) the linear momentum balance equation for the solid, water and gas phase are respectively

$$\mathrm{div}\boldsymbol{t}^s + [1-n]\rho^s\boldsymbol{g} + [1-n]\rho^s\hat{\boldsymbol{t}}^s = \boldsymbol{0} \tag{56}$$

$$\mathrm{div}\boldsymbol{t}^w + nS_w\rho^w\boldsymbol{g} + nS_w\rho^w[\hat{\boldsymbol{t}}^w + \boldsymbol{e}^w] = \boldsymbol{0} \tag{57}$$

$$\mathrm{div}\boldsymbol{t}^g + nS_g\rho^g\boldsymbol{g} + nS_g\rho^g[\hat{\boldsymbol{t}}^g + \boldsymbol{e}^g] = \boldsymbol{0}. \tag{58}$$

The linear momentum balance equation for the mixture

$$\mathrm{div}(\boldsymbol{t}^s + \boldsymbol{t}^w) + \rho\boldsymbol{g} = \boldsymbol{0} \tag{59}$$

is obtained by summation of (56), (57) and (58) because of the constraint (25) and taking into account of the passive air phase assumption, thus neglecting the term $\mathrm{div}\boldsymbol{t}^g$ and the gas density $\rho^g$ with respect to the water density.

In eq. (59) $\rho(\boldsymbol{x}, t)$ is the density of the mixture

$$\rho = [1-n]\rho^s + nS_w\rho^w \tag{60}$$

and $\boldsymbol{t}^s + \boldsymbol{t}^w = \boldsymbol{\sigma}$ is the total Cauchy stress, which can be decomposed into the effective and pressure parts following the principle of effective stress

$$\boldsymbol{\sigma} = \boldsymbol{\sigma}' - S_w p^w \boldsymbol{1} \tag{61}$$

where $\boldsymbol{\sigma}'(\boldsymbol{x}, t)$ is the modified effective Cauchy stress tensor, also called Bishop's stress tensor in soil mechanics. The linear momentum balance equation of the mixture in terms of total Cauchy stress assumes the form

$$\mathrm{div}\boldsymbol{\sigma} + \rho\boldsymbol{g} = \boldsymbol{0} \tag{62}$$

Using the constitutive equation (29) for $nS_\pi\rho^\pi\hat{\boldsymbol{t}}^\pi$, $(\pi = w, g)$ and the definition (30) of $\boldsymbol{t}^\pi$, the linear momentum balance equation for water (57) and gas (58) gives the Darcy's law

$$nS_\pi\boldsymbol{v}^{\pi s} = \frac{\boldsymbol{k}k^{r\pi}}{\mu^\pi} \cdot [-\,\mathrm{grad}p^\pi + \rho^\pi\boldsymbol{g}] \tag{63}$$

for the $\pi$-fluid, where $k^{r\pi} = k^{r\pi}(\boldsymbol{x}, t)$ is the relative permeability which is an experimentally determined function of the capillary pressure. This law is valid for the transport of the $\pi$-fluid in slow phenomena when the thermal effects are negligible. In the following, due to the passive air phase assumption, only the Darcy's for the water will be used. Moreover, the equilibrium equation for the fluid pressures, eq. (36), is simplified as follows

$$p^c \cong -p^w \tag{64}$$

which states that capillary pressures can be approximated as pore water tractions. Hence the water pressure can change in sign, which means that a partially saturated zone is developing in the porous medium. The effect of the capillary pressure on the stiffness of the medium is taken into account by the constitutive laws for $S_w(p^c)$ and $k^{rw}(p^c)$.
As a consequence of the above assumptions, the independent fields of the model are the

solid displacements $\boldsymbol{u}(\boldsymbol{x},t)$ and the water pressure $p^w(\boldsymbol{x},t)$.
In case of fully saturated conditions, $S_w = 1$ and $k^{rw} = 1$ and hence eqs. (60), (61) and (63) are reduced to those of the saturated model.

The Lagrangian counterpart of the mixture balance equations (52) and (59) in terms of material coordinates is now presented. The linear momentum balance equation is obtained using the properties that the total $1^{th}$ Piola-Kirchhoff stress tensor $\boldsymbol{P}(\boldsymbol{X}^s,t)$ can be viewed as the Piola Transform of the second leg of the total Cauchy stress tensor $\boldsymbol{\sigma}(\boldsymbol{x},t)$ [14]

$$P^{aB} = J^s \Big[F^{s-1}\Big]^B_b \sigma^{ab} \tag{65}$$

Multiplying (59) by the jacobian $J^s$, and using the Piola Identity $\mathrm{Div}^s \boldsymbol{P} = J^s \,\mathrm{div}\boldsymbol{\sigma}$ and the relation $J^s\rho = \rho_0$, the linear momentum balance equation of the mixture in material setting is

$$\mathrm{Div}^s \boldsymbol{P} + \rho_0 \boldsymbol{g} = \boldsymbol{0} \tag{66}$$

where ' $\mathrm{Div}^s$' is the divergence operator with respect to material co-ordinates of the solid, and

$$\begin{aligned}\rho_0(\boldsymbol{X}^s,t) = \rho_0^i(\boldsymbol{X}^s,t_0) + S_w(\boldsymbol{X}^s,t)[J^s(\boldsymbol{X}^s,t)-1]\rho^w(\boldsymbol{X}^s,t_0)+\\ +n_0(\boldsymbol{X}^s,t_0)[S_w(\boldsymbol{X}^s,t) - S_{w0}(\boldsymbol{X}^s,t_0)]\rho^w(\boldsymbol{X}^s,t_0)\end{aligned} \tag{67}$$

is the pull back of the mass density of the mixture $\rho(\boldsymbol{x},t)$, in which $n_0(\boldsymbol{X}^s,t_0)$ and $S_{w0}(\boldsymbol{X}^s,t_0)$ are the initial porosity and water saturation in the reference configuration.

The total $1^{th}$ Piola-Kirchhoff stress tensor $\boldsymbol{P}(\boldsymbol{X}^s,t)$ results in an additive decomposition into effective $\boldsymbol{P'}(\boldsymbol{X}^s,t)$ and water pressure parts using the Terzaghi's principle in the form

$$\boldsymbol{P} = \boldsymbol{P'} - J^s S_w p^w [\boldsymbol{F}^s]^{-T} \qquad \text{with} \qquad \boldsymbol{P'} = J^s \boldsymbol{\sigma'} [\boldsymbol{F}^s]^{-T} \tag{68}$$

The mass balance equation of the mixture in material co-ordinates

$$\mathrm{Div}^s(\bar{\boldsymbol{V}}^s + N S_w \bar{\boldsymbol{V}}^{ws}) = 0 \tag{69}$$

is obtained in similar way multiplying the spatial equation (52) by the jacobian $J^s$ and making use of the Piola Identity applied to the velocities $\boldsymbol{v}^s$ and $nS_w\boldsymbol{v}^{ws}$

$$\mathrm{Div}^s \bar{\boldsymbol{V}}^s = J^s \,\mathrm{div}\boldsymbol{v}^s \qquad \mathrm{Div}^s(N S_W \bar{\boldsymbol{V}}^{ws}) = J^s \,\mathrm{div}(n S_w \boldsymbol{v}^{ws}) \tag{70}$$

where $\bar{\boldsymbol{V}}^{ws}$ is the Piola Transform of $\boldsymbol{v}^{ws}$. $N(\boldsymbol{X}^s,t)$ and $S_W(\boldsymbol{X}^s,t)$ are the pull back of $n(\boldsymbol{x},t)$ and $S_w(\boldsymbol{x},t)$, respectively, with $n(\boldsymbol{x},t) = n(\boldsymbol{x}(\boldsymbol{X}^s),t) = N(\boldsymbol{X}^s,t)$ and $S_w(\boldsymbol{x},t) = S_w(\boldsymbol{x}(\boldsymbol{X}^s),t) = S_W(\boldsymbol{X}^s,t)$.

### 3.3 Constitutive Equation for the Solid Skeleton

The elasto-plastic behaviour of the solid skeleton at finite strain is based on the multiplicative decomposition of the deformation gradient $\boldsymbol{F}^s(\boldsymbol{X}^s, t)$ into an elastic and plastic part originally proposed by Lee [15] for crystals

$$\boldsymbol{F}^s = \boldsymbol{F}^{se}\boldsymbol{F}^{sp}. \tag{71}$$

This decomposition states the existence of a intermediate stress free configuration (Figure 3) and its validity has been suggested for cohesive-frictional soils by Nemat-Nasser [16], where the plastic part of the deformation gradient is viewed as an internal variable related to the amount of slipping, crushing, yielding and, for plate like particles, plastic bending of the granules comprising the soil.

In this section the superscript ' $^s$ ' will be neglected and the symbol ' $\dot{}$ ' will be used for the material time derivative with respect to the solid skeleton instead of $D^s/Dt$ (as well as in the remaining part of the paper).

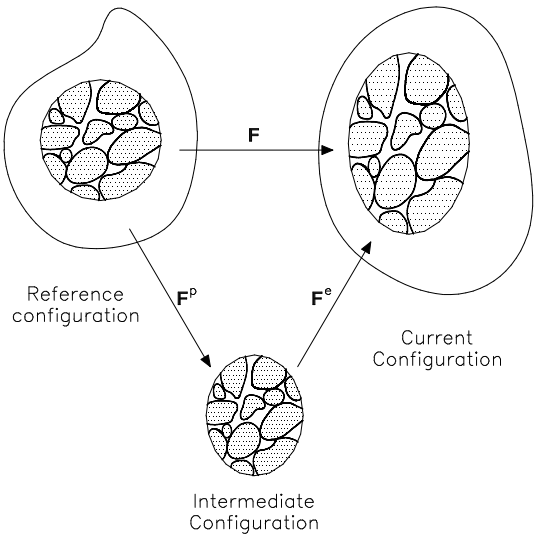


Figure 3: Illustration of the local multiplicative decomposition of the solid deformation gradient $\boldsymbol{F}$.

The spatial formulation is used in this section. The treatment of the isotropic elasto-plastic behaviour for the solid skeleton based on the product formula algorithm proposed for the single phase material by Simo [17] is now briefly summarised.

The effective Kirchhoff stress tensor $\boldsymbol{\tau}'(\boldsymbol{x}, t) = J\boldsymbol{\sigma}'(\boldsymbol{x}, t)$ and the logarithmic principal values of the elastic left Cauchy-Green strain tensor $\epsilon_A(\boldsymbol{x}, t)$ are used. In the present sub-section also the prime ' $'$ ' for the effective stress tensor will be neglected. The yield function restricting the stress state is developed in the form of von Mises and Drucker-Prager [18], to take into account the behaviour of clays under undrained conditions and the dilatant/contractant behaviour of dense or loose sands, respectively. The return mapping and the consistent tangent operator is developed, soloving the singular behaviour of the

Drucker-Prager yield surface in the zone of the apex using the concept of multisurface plasticity.

The elastic behaviour of the solid skeleton is assumed to be governed by an hyperelastic free energy $\psi(\boldsymbol{x}, t)$ function in the form

$$\psi = \psi(\boldsymbol{b}^e, \xi) \tag{72}$$

dependent of the elastic left Cauchy-Green strain tensor, $\boldsymbol{b}^e(\boldsymbol{x}, t) = \boldsymbol{F}^e \cdot [\boldsymbol{F}^e]^{-1}$, and the internal strain like variable, $\xi(\boldsymbol{x}, t)$, equivalent plastic strain. The second law of thermodynamic yields, under the restriction of isotropy, the constitutive relations

$$\boldsymbol{\tau} = 2\frac{\partial \psi}{\partial \boldsymbol{b}^e} \cdot \boldsymbol{b}^e \qquad\qquad q = -\frac{\partial \psi}{\partial \xi} \tag{73}$$

and the remaining dissipation inequality

$$-\frac{1}{2}\boldsymbol{\tau} : \left[ [L_v \boldsymbol{b}^e] \cdot [\boldsymbol{b}^e]^{-1} \right] + q\dot{\xi} \geq 0 \tag{74}$$

where $L_v \boldsymbol{b}^e = \dot{\boldsymbol{b}}^e - \boldsymbol{l} \cdot \boldsymbol{b}^e - \boldsymbol{b}^e \cdot \boldsymbol{l}^T$ is the Lie derivative of the elastic left Cauchy-Green strain tensor $\boldsymbol{b}^e(\boldsymbol{x}, t)$.

The evolution equations for the rate terms of the dissipation inequality (74) can be derived from the postulate of the maximum plastic dissipation in the case of associative flow rules [17]

$$-\frac{1}{2} L_v \boldsymbol{b}^e = \dot{\gamma} \frac{\partial F}{\partial \boldsymbol{\tau}} \boldsymbol{b}^e \tag{75}$$

$$\dot{\xi} = \dot{\gamma} \frac{\partial F}{\partial q} \tag{76}$$

subjected to the classical loading-unloading conditions in Kuhn-Tucker form

$$\dot{\gamma} \geq 0, \quad F = F(\boldsymbol{\tau}, q) \leq 0, \quad \dot{\gamma} F = 0 \tag{77}$$

where $\dot{\gamma}$ is the plastic multiplier and $F = F(\boldsymbol{\tau}, q)$ the isotropic yield function.
For the computation classical elastoplastic models have been selected. In particular, the Drucker-Prager and the von Mises yield functions with linear isotropic hardening have been used in the form, respectively,

$$F(p, \boldsymbol{s}, \xi) = 3\alpha_F p + \|\boldsymbol{s}\| - \beta_F \sqrt{\frac{2}{3}} [c_0 + h\xi] \tag{78}$$

and

$$F(\boldsymbol{s}, \xi) = \|\boldsymbol{s}\| - \sqrt{\frac{2}{3}} [\sigma_0 + h\xi] \tag{79}$$

in which $p = \frac{1}{3}[\boldsymbol{\tau} : \mathbf{1}]$ is the mean effective Kirchhoff pressure, $\|\boldsymbol{s}\|$ is the $L_2$ norm of the deviator effective Kirchhoff stress tensor $\boldsymbol{\tau}$, $c_0$ is the initial apparent cohesion of the Drucker-Prager model, $\alpha$ and $\beta$ are two parameter related to the friction angle $\phi$ of the soil

$$\alpha_F = 2\frac{\sqrt{\frac{2}{3}}\sin\phi}{3-\sin\phi} \qquad \beta_F = \frac{6\cos\phi}{3-\sin\phi} \tag{80}$$

$h$ the hardening/softening modulus and $\sigma_0$ is the yield stress in the von Mises law.

### 3.4 Algorithmic Formulation for Elastoplasticity

The problem of the calculation of $\boldsymbol{b}^e, \xi$ and $\boldsymbol{\tau}$ is solved by an operator split into an elastic predictor and plastic corrector [19]. The calculation of the trial elastic state $(\bullet)^{tr}$ is based on the freezing of the plastic flow at time $t_{n+1}$. The $[\boldsymbol{b}^e_{n+1}]^{tr}$ is hence the push forward of $\boldsymbol{b}^e_n$ by means of the relative deformation gradient $\boldsymbol{f}_{n+1} = \frac{\partial \boldsymbol{\chi}_{n+1}}{\partial \boldsymbol{x}_n} = \mathbf{1} + \text{grad}\Delta\boldsymbol{u}_{n+1}$, i.e.

$$[\boldsymbol{b}^e_{n+1}]^{tr} = \boldsymbol{f}_{n+1}\boldsymbol{b}^e_n\boldsymbol{f}^T_{n+1} \tag{81}$$

with $\xi^{tr}_{n+1} = \xi_n$ , where $\Delta\boldsymbol{u}_{n+1}$ is the incremental displacement in the time interval $[t_n, t_{n+1}]$.
The same value can also be obtained from the reference configuration by the push forward of $[\boldsymbol{C}^p_n]^{-1}$ by means of $\boldsymbol{F}_{n+1}$

$$[\boldsymbol{b}^e_{n+1}]^{tr} = \boldsymbol{F}_{n+1}[\boldsymbol{C}^p_n]^{-1}\boldsymbol{F}^T_{n+1} \tag{82}$$

The corresponding trial elastic stress is obtained from the hyperelastic free energy function as

$$\boldsymbol{\tau}^{tr}_{n+1} = 2\left[\frac{\partial\psi}{\partial\boldsymbol{b}^e}\cdot\boldsymbol{b}^e\right]_{\boldsymbol{b}^e=[\boldsymbol{b}^e_{n+1}]^{tr}} = 2\frac{\partial\psi}{\partial\boldsymbol{b}^e}\bigg|_{\boldsymbol{b}^e=[\boldsymbol{b}^e_{n+1}]^{tr}}\cdot[\boldsymbol{b}^e_{n+1}]^{tr} \tag{83}$$

If this trial state is admissible, it does not violate the inequality $F^{tr}_{n+1} = F(\boldsymbol{\tau}^{tr}_{n+1}, q^{tr}_{n+1}) \leq 0$ and the stress state is hence already computed.

Otherwise the return mapping or plastic corrector algorithm is applied to satisfy the condition $F_{n+1} = 0$. Since during this phase the spatial position $\boldsymbol{\chi} = \boldsymbol{\chi}^{tr}$ is held fixed and thus $\boldsymbol{l} \equiv \mathbf{0}$, the evolution equation for the elastic left Cauchy-Green strain tensor becomes

$$L_v\boldsymbol{b}^e = -2\dot{\gamma}\frac{\partial F}{\partial\boldsymbol{\tau}}\boldsymbol{b}^e \quad \text{with} \quad L_v\boldsymbol{b}^e\bigg|_{\boldsymbol{\chi}=\boldsymbol{\chi}^{tr}} = \dot{\boldsymbol{b}}^e \tag{84}$$

This first order differential equation is solved by the product formula algorithm (exponential approximation of the solution, having $1th$ order accuracy) during the time interval $[t_n, t_{n+1}]$ [17]

$$\boldsymbol{b}^e_{n+1} \cong \exp\left(-2\Delta\gamma\frac{\partial F}{\partial\boldsymbol{\tau}}\right)\bigg|_{n+1}\cdot[\boldsymbol{b}^e_{n+1}]^{tr}. \tag{85}$$

It should now be noted that $\boldsymbol{b}^e_{n+1}$ commutes with $\boldsymbol{\tau}_{n+1}$ due to the assumption of isotropy and that $[\boldsymbol{b}^e_{n+1}]^{tr}$ and its principal axis are held fixed during the return mapping; the spectral decomposition of $[\boldsymbol{b}^e_{n+1}]^{tr}, \boldsymbol{b}^e_{n+1}$ and $\boldsymbol{\tau}_{n+1}$ can hence be written with the same eigenbases

$$[\boldsymbol{b}^e]^{tr} = \sum_{A=1}^{3} [\lambda^{tr}_{Ae}]^2 \boldsymbol{n}^{tr}_A \otimes \boldsymbol{n}^{tr}_A \qquad \boldsymbol{b}^e = \sum_{A=1}^{3} [\lambda_{Ae}]^2 \boldsymbol{n}^{tr}_A \otimes \boldsymbol{n}^{tr}_A$$
$$\boldsymbol{\tau} = \sum_{A=1}^{3} \tau_A \boldsymbol{n}^{tr}_A \otimes \boldsymbol{n}^{tr}_A \tag{86}$$

Using (86) the product formula (85) can be written in principal values in the form

$$[\lambda_{Ae}]^2 = \exp\left(-2\Delta\gamma \frac{\partial F}{\partial \tau_A}\right)\Bigg|_{n+1} [\lambda^{tr}_{Ae}]^2. \tag{87}$$

Taking the logarithm of (87) the following important *additive* decomposition of the *log* strain measure in elastic and plastic parts is obtained [17]

$$\varepsilon^{tr}_{Ae_{n+1}} = \varepsilon_{Ae_{n+1}} + \Delta\gamma \frac{\partial F}{\partial \tau_A}\Bigg|_{n+1} \tag{88}$$

in which $\varepsilon_{Ae}$ are the principal logarithmic elastic strain $\varepsilon_{Ae} = ln\lambda_A$. This is a very important consequence of the utilised model because it permits to use the return mapping of the elasto-plasticity developed for the linear case [19]. From the knowledge of $\Delta\gamma$ the equivalent plastic strain is computed by the backward Euler integration of eq. (76)

$$\xi_{n+1} \cong \xi_n + \Delta\gamma \frac{\partial F}{\partial q}\Bigg|_{n+1} \tag{89}$$

The principal Kirchhoff stress components are then computed by the hyperelastic constitutive law

$$\tau_A = 2\lambda_{Ae} \frac{\partial \psi}{\partial \lambda_{Ae}} = \frac{\partial \psi}{\partial \varepsilon_{Ae}} \tag{90}$$

where the free energy $\psi = \hat{\psi}(\varepsilon_{Ae}, \xi)$ is now written as function of the principal elastic logarithmic strain components and the equivalent plastic strain (for isotropic linear hardening)

$$\hat{\psi} = \frac{L}{2}[\varepsilon_{1e} + \varepsilon_{2e} + \varepsilon_{3e}]^2 + G[\varepsilon^2_{1e} + \varepsilon^2_{2e} + \varepsilon^2_{3e}] + \frac{1}{2}h\xi^2 \tag{91}$$

where $L$ and $G$ are the elastic Lame' constants and $h$ the linear hardening modulus.

The strain energy function $W = \rho_{s0}\hat{\psi}$ of the solid skeleton associated to $\hat{\psi}$ and used in this paper is the original one proposed by Simo [17]. It is valid only for moderate large elastic

strain because it does not satisfy the convexity condition for very large elastic strains [20] but it has been used here because the soils behaves with moderate elastic strains. Some useful remarks related to the use of this strain energy function can be found e.g. in [21], in which it has been shown that the finite element computation loses stability at finite elastic strains.

## 4 Weak Form: Variational Approach

The weak form of the spatial governing equations presented in the previous section is now derived obtaining the variational equations formally equivalent to the initial boundary value problem given by the governing equation and the boundary conditions. This means that the governing equations (52) and (59) are multiplied by independent weighting functions that vanish on the boundary in which Dirichlet boundary conditions are applied and are then integrated over the spatial domain, $B$, with boundary, $\partial B$. The linear momentum balance equation of the binary porous media (59) is hence weighted on the domain by the test function $\delta \boldsymbol{u}_s$ corresponding to the solid displacement (or virtual displacement) in the form

$$\int_B [\,\mathrm{div}\boldsymbol{\sigma} + \rho \boldsymbol{g}] \cdot \delta \boldsymbol{u}_s dv = 0 \quad \forall \delta \boldsymbol{u}_s \tag{92}$$

Applying partial integration and the Green's Theorem in the form (e.g. [14], [20])

$$\int_B \mathrm{div}\boldsymbol{\sigma} \cdot \delta \boldsymbol{u}_s dv = -\int_B \boldsymbol{\sigma} : \mathrm{grad}\delta \boldsymbol{u}_s dv + \int_{\partial B} \bar{\boldsymbol{t}} \cdot \delta \boldsymbol{u}_s ds \tag{93}$$

to the divergence part of (92) and taking into account the boundary conditions, this equation is transformed into the weak form

$$\begin{aligned} &-\int_B [\boldsymbol{\sigma}' - S_w p^w \mathbf{1}] : \mathrm{grad}\delta \boldsymbol{u}_s dv + \\ &+\int_B \rho \boldsymbol{g} \cdot \delta \boldsymbol{u}_s dv + \int_{\partial B} \bar{\boldsymbol{t}} \cdot \delta \boldsymbol{u}_s ds = 0 \quad \forall \delta \boldsymbol{u}_s \end{aligned} \tag{94}$$

where the effective stress principle (61) has been introduced. Using the relation $\mathrm{div}\delta \boldsymbol{u}_s = \mathrm{grad}\delta \boldsymbol{u}_s : \mathbf{1}$, the previous weak form is transformed in

$$\begin{aligned} &-\int_B \boldsymbol{\sigma}' : \mathrm{grad}\delta \boldsymbol{u}_s dv + \int_B S_w p^w \,\mathrm{div}\delta \boldsymbol{u}_s dv + \\ &+\int_B \rho \boldsymbol{g} \cdot \delta \boldsymbol{u}_s dv + \int_{\partial B} \bar{\boldsymbol{t}} \cdot \delta \boldsymbol{u}_s ds = 0 \quad \forall \delta \boldsymbol{u}_s \end{aligned} \tag{95}$$

The weak form of the mixture mass balance equation (52) is obtained in a similar way, introducing the Darcy's law (63) and using the test function $\delta p^w$ corresponding to $p^w$ (or virtual water pressure)

$$\int_B \mathrm{div}\boldsymbol{v}^s \delta p^w dv + \underline{\int_B \mathrm{div}\left(\frac{\boldsymbol{k}k^{rw}}{\mu^w}\cdot[-\mathrm{grad}p^w + \rho^w \boldsymbol{g}]\right)\delta p^w dv} = 0 \quad \forall \delta p^w \tag{96}$$

Applying the Green's Theorem to the underlined term of the previous equation, the following is obtained,

$$\begin{aligned}\int_B \mathrm{div}\boldsymbol{v}^s \delta p^w dv + \int_B \left[\frac{\boldsymbol{k}k^{rw}}{\mu^w}\cdot[\,\mathrm{grad}p^w - \rho^w \boldsymbol{g}]\right]\cdot \mathrm{grad}\delta p^w dv + \\ + \int_{\partial B} q^w \delta p^w ds = 0 \quad \forall \delta p^w\end{aligned} \tag{97}$$

where $q^w(\boldsymbol{x}, t)$ is the water flow draining through the surface $\partial B$.

**Remarks**: it can be observed that the weak forms (95) and (97) are very similar to those of the geometrically linear theory, e.g. [6], by substituting the deformed integration domain, $B$, with the undeformed one, $B_0$. Moreover, in the small strain theory $\mathrm{div}\boldsymbol{v}^s = \dot{\boldsymbol{\varepsilon}} : \mathbf{1}$ where $\boldsymbol{\varepsilon}$ is the small strain tensor of the solid skeleton, while in finite strain $\mathrm{div}\boldsymbol{v}^s = \dot{J}^s/J^s$. In small strain theory the additive decomposition of the strain tensor $\boldsymbol{\varepsilon}$ in elastic and plastic parts is also possible, thus rendering the computation of the constitutive tangent operator in the linearisation of the weak form particularly easy.

## 5 Time Discretisation

Time integration of the weak form of the mass balance equation (97) over a finite time step $\Delta t = t_{n+1} - t_n$ is necessary because of the time dependent term $\mathrm{div}\boldsymbol{v}^s$.

The Generalised Trapezoidal Method is here used, as shown for instance in [6]. Because of the dependency of the integration domain from the time, we rewrite the weak forms (95) and (97) with respect to the undeformed domain as follows:

$$\begin{aligned}\int_{B_0} [\boldsymbol{\tau}' - J^s S_w p^w \mathbf{1}] : \mathrm{grad}\delta \boldsymbol{u}_s dV - \int_{B_0} \rho_0 \boldsymbol{g}\cdot\delta\boldsymbol{u}_s dV - \\ - \int_{\partial B_0} \bar{\boldsymbol{T}}\cdot\delta\boldsymbol{u}_s dA = 0 \quad \forall \delta\boldsymbol{u}_s\end{aligned} \tag{98}$$

$$\int_{B_0} J^s \, \mathrm{div}\boldsymbol{v}^s \delta p^w dV + \int_{B_0} \left[ J^s \frac{\boldsymbol{k} k^{rw}}{\mu^w} \cdot [\, \mathrm{grad} p^w - \rho^w \boldsymbol{g}] \right] \cdot \, \mathrm{grad} \delta p^w dV + \\ + \int_{\partial B_0} Q^w \delta p^w dA = 0 \quad \forall \delta p^w \tag{99}$$

where $\boldsymbol{\tau}'$ is the modified effective Kirchhoff stress tensor and $\bar{\boldsymbol{T}} = \boldsymbol{P} \cdot \boldsymbol{N}$ and $Q^w = NS_W \bar{\boldsymbol{V}}^{ws} \cdot \boldsymbol{N}$ are, respectively, the traction vector and the water flow computed with respect to the undeformed configuration. The form of eqs. (98) and (99) is also useful for the subsequent linearisation, because it will be easily performed with respect to the undeformed (fixed) domain.

Equation (99) is now rewritten at time $t_{n+1}$ using the relationships

$$\dot{J}^s_{n+\beta} = \frac{J^s_{n+1} - J^s_n}{\Delta t} \tag{100}$$

$$(\bullet)_{n+\beta} = [1-\beta](\bullet)_n + \beta(\bullet)_{n+1} = (\bullet)_n + \beta[(\bullet)_{n+1} - (\bullet)_n] \tag{101}$$

with $\beta = (0, 1]$, obtaining

$$\int_{B_0} [J^s_{n+1} - J^s_n] \delta p^w dV - \Delta t \int_{B_0} [J^s \boldsymbol{v}^D \cdot \, \mathrm{grad} \delta p^w]_{n+\beta} dV + \\ + \Delta t \int_{\partial B_0} Q^w_{n+\beta} \delta p^w dA = 0 \quad \forall \delta p^w \tag{102}$$

where $\boldsymbol{v}^D = -\frac{\boldsymbol{k} k^{rw}}{\mu^w} \cdot (\, \mathrm{grad} p^w - \rho^w \boldsymbol{g})$ is the Darcy's velocity of the water.

The weak form of the linear momentum balance equation (98) is directly written at time $t_{n+1}$ because it is time independent

$$\int_{B_0} \left[ [\boldsymbol{\tau}' - J^s S_w p^w \mathbf{1}] : \, \mathrm{grad} \delta \boldsymbol{u}_s \right]_{n+1} dV - \int_{B_0} \rho_{0_{n+1}} \boldsymbol{g} \cdot \delta \boldsymbol{u}_s dV - \\ - \int_{\partial B_0} \bar{\boldsymbol{T}}_{n+1} \cdot \delta \boldsymbol{u}_s dA = 0 \quad \forall \delta \boldsymbol{u}_s \tag{103}$$

Linearised analysis of accuracy and stability suggest the use of $\beta \geq \frac{1}{2}$. In the examples section, implicit one-step time integration has been performed ($\beta = 1$).

The weak forms (102) and (103) represent a non-linear coupled equations system where the non linearities are introduced by the finite kinematics and the constitutive laws.

## 6 Consistent Linearisation

The non linear equation system (102, 103) can be written in the following compact form

$$\boldsymbol{G}(\boldsymbol{\chi}^s, \boldsymbol{\eta}) = \boldsymbol{0}, \quad \text{where} \quad \boldsymbol{\eta} = [\delta \boldsymbol{u}_s, \delta p^w]^T. \tag{104}$$

For its numerical solution iterative methods have to be employed and the linearisation at $\bar{\boldsymbol{\chi}}^s$ is hence necessary

$$\boldsymbol{G}(\bar{\boldsymbol{\chi}}^s, \boldsymbol{\eta}, \Delta \boldsymbol{u}) \cong \boldsymbol{G}(\bar{\boldsymbol{\chi}}^s, \boldsymbol{\eta}) + D\boldsymbol{G}(\bar{\boldsymbol{\chi}}^s, \boldsymbol{\eta}) \cdot \Delta \boldsymbol{u} \cong \boldsymbol{0} \tag{105}$$

where $\Delta \boldsymbol{u} = [\Delta \boldsymbol{u}_s, \Delta p^w]^T$ and $D\boldsymbol{G} \cdot \Delta \boldsymbol{u} = \frac{d}{d\alpha} \boldsymbol{G}(\bar{\boldsymbol{\chi}}^s + \alpha \Delta \boldsymbol{u})|_{\alpha=0}$ is the directional derivative or Gateaux derivative of $\boldsymbol{G}$ at $\bar{\boldsymbol{\chi}}^s$ in the direction of $\Delta \boldsymbol{u}$ (e.g. [14], [22] for single phase material). Since the equation system $\boldsymbol{G}$ is composed of the weak form of the linear momentum balance equation ($G_{LBE}$) and of mass balance equation ($G_{MBE}$), then

$$D\boldsymbol{G} \cdot \Delta \boldsymbol{u} = \begin{bmatrix} DG_{LBE} \cdot \Delta \boldsymbol{u}_s + DG_{LBE} \cdot \Delta p^w \\ \\ DG_{MBE} \cdot \Delta \boldsymbol{u}_s + DG_{MBE} \cdot \Delta p^w \end{bmatrix}. \tag{106}$$

Using the symbol $(\bullet)_{n+1}^{k+1}$ to indicate the current iteration in the current time step, the linearisation on the configuration $(\bullet)_{n+1}^{k}$ is written as

$$D\boldsymbol{G}_{n+1}^{k} \cdot \Delta \boldsymbol{u}_{n+1}^{k+1} = -\boldsymbol{G}_{n+1}^{k} \tag{107}$$

and the solution vector $\boldsymbol{u} = [\boldsymbol{u}_s, p^w]^T$ is then updated by the incremental relationship

$$\boldsymbol{u}_{n+1}^{k+1} = \boldsymbol{u}_{n+1}^{k} + \Delta \boldsymbol{u}_{n+1}^{k+1} \tag{108}$$

For an efficient numerical performance of the scheme (107) the consistent linearisation is applied [22] in which the linearisation of the integrated constitutive equation (86) plays a central role (this concept was first pointed out in [23] for the geometrically linear case).

The linearisation of eqs. (102) and (103), performed in the undeformed configuration, $B_0$, and then pushed forward in the deformed configuration, $B$, gives the following result:

- for the linear momentum balance equation

$$\begin{aligned}
&\int_B [\,\mathrm{grad}\delta\boldsymbol{u}_s : \boldsymbol{c}^{ep} : \mathrm{sym}(\,\mathrm{grad}\Delta\boldsymbol{u}_s) + \boldsymbol{\sigma}' : \mathrm{grad}^T\delta\boldsymbol{u}_s\,\mathrm{grad}\Delta\boldsymbol{u}_s]dv + \\
&+\int_B S_w p^w\,\mathrm{grad}\delta\boldsymbol{u}_s : [\,\mathrm{grad}^T\Delta\boldsymbol{u}_s - \mathrm{div}\Delta\boldsymbol{u}_s\mathbf{1}]dv - \\
&-\int_B \rho^w S_w\delta\boldsymbol{u}_s\cdot\boldsymbol{g}\,\mathrm{div}\Delta\boldsymbol{u}_s dv - \int_B [p^w\frac{\partial S_w}{\partial p^w} + S_w]\,\mathrm{div}\delta\boldsymbol{u}_s\Delta p^w dv
\end{aligned} \tag{109}$$

- for the mass balance equation

$$\begin{aligned}
&\int_B \delta p^w\,\mathrm{div}\Delta\boldsymbol{u}_s dv + \beta\Delta t\int_B \frac{kk^{rw}}{\mu^w}\,\mathrm{grad}\delta p^w\cdot\,\mathrm{grad}\Delta p^w dv + \\
&+\beta\Delta t\int_B \mathrm{grad}\delta p^w\cdot\left[[\frac{1-n}{k}\frac{\partial k}{\partial n}+1]\frac{kk^{rw}}{\mu^w}[\,\mathrm{grad}p^w - \rho^w\boldsymbol{g}]\,\mathrm{div}\Delta\boldsymbol{u}_s\right]dv - \\
&-\beta\Delta t\int_B \mathrm{grad}\delta p^w\cdot\left[\frac{2kk^{rw}}{\mu^w}\,\mathrm{sym}(\,\mathrm{grad}\Delta\boldsymbol{u}_s)\cdot\,\mathrm{grad}p^w\right]dv + \\
&+\beta\Delta t\int_B \mathrm{grad}\delta p^w\cdot\left[\frac{kk^{rw}}{\mu^w}\rho^w\,\mathrm{grad}\Delta\boldsymbol{u}_s\cdot\boldsymbol{g}\right]dv + \\
&+\beta\Delta t\int_B \frac{k}{\mu^w}\frac{\partial k^{rw}}{\partial p^w}\,\mathrm{grad}p^w\cdot\,\mathrm{grad}\delta p^w\Delta p^w dv
\end{aligned} \tag{110}$$

In the directional derivative $DG_{LBE}\cdot\Delta\boldsymbol{u}_s$ the term

$$\int_B [\,\mathrm{grad}\delta\boldsymbol{u}_s : \boldsymbol{c}^{ep} : \mathrm{sym}(\,\mathrm{grad}\Delta\boldsymbol{u}_s) + \boldsymbol{\sigma}' : \mathrm{grad}^T\delta\boldsymbol{u}_s\,\mathrm{grad}\Delta\boldsymbol{u}_s]dv \tag{111}$$

contains $\boldsymbol{c}^{ep}$, the spatial constitutive operator following the linearisation of (86)

$$\begin{aligned}
\boldsymbol{c}^{ep}_{n+1} = &\sum_{A=1}^{3}\sum_{B=1}^{3} a^{ep}_{AB_{n+1}}[\boldsymbol{n}^{tr}_A\otimes\boldsymbol{n}^{tr}_A]\otimes[\boldsymbol{n}^{tr}_B\otimes\boldsymbol{n}^{tr}_B] + \\
&+2\sum_{A=1}^{3}\tau_{A_{n+1}}\boldsymbol{c}^{tr(A)}_{n+1}
\end{aligned} \tag{112}$$

It is useful to remark that in (112) only the second order tensor $\boldsymbol{a}^{ep} = \partial\tau_A/\partial\varepsilon_B^{tr}$ depends on the specific model of plasticity and the structure of the return mapping algorithm in principal stretches, while the tensors $\boldsymbol{c}_{n+1}^{tr(A)}$ and $\boldsymbol{n}_A^{tr} \otimes \boldsymbol{n}_A^{tr}$ are independent of the specific plastic model used. Moreover it is easy to proof that the moduli $\boldsymbol{a}^{ep}$ have a form identical to the algorithmic elastoplastic tangent moduli of the infinitesimal theory [17]. The expression for $\boldsymbol{c}_{n+1}^{tr(A)}$ can obtained by linearisation of the eigenbases dyadic $\boldsymbol{n}_A^{tr} \otimes \boldsymbol{n}_A^{tr}$ in the spatial setting

$$\boldsymbol{c}_{n+1}^{tr(A)} = \frac{\partial[\boldsymbol{n}_A^{tr} \otimes \boldsymbol{n}_A^{tr}]}{\partial \boldsymbol{g}} \tag{113}$$

where $\boldsymbol{g}$ is the spatial metric, or by pull back [14] of $\boldsymbol{n}_A^{tr} \otimes \boldsymbol{n}_A^{tr}$, subsequent to linearisation in the material setting using the relations e.g. of [24] and then by push forward of the linearisation in spatial setting. The expression for the 2-D problem is derived in the next subsection.

### 6.1 Drucker-Prager Model with Linear Isotropic Hardening: Return Mapping and Algorithmic Tangent Moduli with Apex Solution

Originally the return mapping algorithm was developed for $J_2$-plasticity. Extension of this method to the Drucker-Prager model can be made taking into account a special treatment of the corner region using the concept of multi-surface plasticity, as developed in [25] in case of perfect plasticity and deviatoric non-associative plasticity. In this paper the return mapping and the algorithmic tangent moduli will be obtained for isotropic linear hardening/softening and volumetric-deviatoric non-associative plasticity. To this end, a plastic potential function $Q(p, \boldsymbol{s}, \xi)$ similar to (78) is defined, where the dilatancy angle $\varphi$ is introduced.

The key idea is based on the fact that the return mapping algorithm developed without any special treatment of the apex region leads to physically meaningless results (i.e. $||\boldsymbol{s}_{n+1}|| < 0$) for a certain range of trial elastic stress. Once the plastic consistency parameter $\Delta\gamma_{n+1}$ is computed by the return mapping, this happens when the following relationship obtained from the updated deviatoric components of the stress tensor

$$||\boldsymbol{s}_{n+1}|| = ||\boldsymbol{s}_{n+1}^{tr}|| - 2G\Delta\gamma_{n+1} \geq 0 \tag{114}$$

is violated. Without going into details, violation of inequality (114) and the consistency condition $F_{n+1} = F(\boldsymbol{\tau}_{n+1}, \xi_{n+1}) = 0$ yields the inequality for which the return mapping needs to be modified, i.e.:

$$p_{n+1}^{tr} > \frac{3\alpha_Q K}{2G}||\boldsymbol{s}_{n+1}^{tr}|| + \frac{\beta_F\sqrt{\frac{2}{3}}}{\alpha_F}\left[\frac{||\boldsymbol{s}_{n+1}^{tr}||}{2G}h\sqrt{1+3\alpha_Q^2} + c_n\right] \tag{115}$$

where the indexes $F$ and $Q$ of $\alpha$ and $\beta$ are referred to the yield and the plastic potential surface, respectively.
In this case, the stress region characterised by (115) may be treated like a corner region in non-smooth multi-surface plasticity. To this end a second yield condition $F_2$ is introduced in addition to (78) as

$$F_2(p,\xi) = 3\alpha_F p - \beta_F \sqrt{\frac{2}{3}}[c_0 + h\xi] \tag{116}$$

which is derived from (78) with the condition $||\boldsymbol{s}|| = 0$ and the plastic evolution equations need to be modified following the Koiter's generalisation introducing a second plastic consistency parameter $\dot{\gamma}_2$ related to $F_2$. Hence the evolution eqs. (75) will be substituted by the generalised plastic evolution laws

$$L_v \boldsymbol{b}^e = -2 \sum_i \dot{\gamma}_i \frac{\partial F_i}{\partial \boldsymbol{\tau}} \boldsymbol{b}^e, \qquad i = 1,2 \tag{117}$$

$$\dot{\xi} = \sum_i \dot{\gamma}_i \frac{\partial F_i}{\partial q}, \qquad i = 1,2 \tag{118}$$

The algorithmic tangent moduli are computed by linearisation of the computed Kirchhoff stress tensor. Two tangent moduli are obtained, the first one valid for the stress state where the Drucker-Prager model is satisfied, i.e. for the stress for which eq. (115) is violated, the second one for the stress state which belongs to the corner region. The computed moduli for the two cases are respectively:

- for the non corner zone:

$$\begin{aligned} \boldsymbol{a}^{ep}_{n+1} = {} & c_1 K \mathbf{1} \otimes \mathbf{1} + 2G \left[ \boldsymbol{I} - \tfrac{1}{3} \mathbf{1} \otimes \mathbf{1} \right] \left[ 1 - \tfrac{2G\Delta\gamma_{n+1}}{||\boldsymbol{s}^{tr}_{n+1}||} \right] - \\ & - \frac{6\alpha_Q K G}{c_2} \mathbf{1} \otimes \boldsymbol{n}^{tr}_{n+1} - \frac{6\alpha_F K G}{c_2} \boldsymbol{n}^{tr}_{n+1} \otimes \mathbf{1} - \\ & - 4G^2 \left[ \frac{1}{c_2} - \frac{\Delta\gamma_{n+1}}{||\boldsymbol{s}^{tr}_{n+1}||} \right] \boldsymbol{n}^{tr}_{n+1} \otimes \boldsymbol{n}^{tr}_{n+1} \end{aligned} \tag{119}$$

where the coefficients $c_1$ and $c_2$ are

$$c_1 = \left[ 1 - \frac{9\alpha_F \alpha_Q K}{c_2} \right], \qquad c_2 = 9\alpha_F \alpha_Q K + 2G + \beta_F h \sqrt{\frac{2}{3}[1 + 3\alpha_Q^2]}$$

- for the corner zone:

$$\boldsymbol{a}^{ep}_{n+1} = \left[ K\mathbf{1}\otimes\mathbf{1} + \frac{K}{2\alpha_Q G(\Delta\gamma_1+\Delta\gamma_2)_{n+1}}\mathbf{1}\otimes\boldsymbol{s}^{tr}_{n+1}\right] c_3 \tag{120}$$

where the coefficient $c_3$ is

$$c_3 = \frac{\alpha_Q\beta_F\sqrt{\frac{2}{3}}h[\Delta\gamma_1+\Delta\gamma_2]_{n+1}}{3\alpha_F K\sqrt{\Delta\gamma_1^2{}_{n+1}+3\alpha_Q^2[\Delta\gamma_1+\Delta\gamma_2]^2_{n+1}}+\alpha_Q\beta_F\sqrt{\frac{2}{3}}h[\Delta\gamma_1+\Delta\gamma_2]_{n+1}}$$

It can be observed that the moduli (120) are non symmetric even for associated plasticity, while (119) are non symmetric only for non associated plasticity. In case of perfect plasticity ($h = 0$) the coefficient $c_3$ and hence the moduli of eq. (120) vanish. In case of geometrically non-linear analysis, this implies that only the geometrical part of the stiffness matrix is activated. Moreover, the moduli (120) are reduced to those of the von Mises model by selecting $\alpha = 0$ and $\beta = 1$.

## 7 Finite Element Discretisation in Space

The suitable spatial Finite Element formulation is derived by applying the well known Galerkin procedure, in which the weighting functions are approximated by the same shape functions used to approximate the driving variables (isoparametric finite elements). This means that the geometry, $\boldsymbol{X}^s$, the current configuration, $\boldsymbol{x}$, the displacement field, $\boldsymbol{u}_s$, the water pressure, $p^w$, the incremental generalised displacement, $\Delta\boldsymbol{u} = [\Delta\boldsymbol{u}_s, \Delta p^w]^T$, and the variations, $\boldsymbol{\eta} = [\delta\boldsymbol{u}_s, \delta p^w]^T$, are interpolated within a finite element by the same type of functions. In the present setting different shape functions are chosen for quantities associated respectively to the solid and the fluid, thus satisfying the LBB condition for the locally undrained case. Standard procedures have been applied, following any text books on FEM. With respect to the small strain case, the discretisation of the spatial form of the linearised system of equations is made taking into account that each quantity is referred to the spatial coordinates, $\boldsymbol{x}$, instead of the coordinates of the undeformed configuration, $\boldsymbol{X}^s$. (In the present formulation quadrilateral $Q_2Q_1$ or $S_2Q_1$ elements have been used for the Liakopoulos' test and the localisation example, respectively). The solid displacement $\boldsymbol{u}(\boldsymbol{x}, t)$ and the water pressure $p^w(\boldsymbol{x}, t)$ are hence expressed in the whole domain by global shape function matrices $\boldsymbol{N}_u(\boldsymbol{x})$ and $\boldsymbol{N}_w(\boldsymbol{x})$ and the nodal value vectors $\bar{\boldsymbol{u}}(t)$ and $\bar{\boldsymbol{p}}(t)$

$$\boldsymbol{u} = \boldsymbol{N}_u\bar{\boldsymbol{u}}, \qquad p^w = \boldsymbol{N}_w\bar{\boldsymbol{p}}. \tag{121}$$

The linearised system of equations (107) in matrix form can be expressed as

$$\begin{bmatrix} \boldsymbol{K}_T + \boldsymbol{K}_{sw}^{geom.} & -c_{sw}\boldsymbol{Q}_{sw} \\ \boldsymbol{Q}_{ws} - \beta\Delta t\boldsymbol{Q}_{sw}^{geom.} & \beta\Delta t\boldsymbol{H} \end{bmatrix} \begin{bmatrix} \Delta\bar{\boldsymbol{u}} \\ \Delta\bar{\boldsymbol{p}} \end{bmatrix} = - \begin{bmatrix} \boldsymbol{G}^u \\ \boldsymbol{G}^p \end{bmatrix} \tag{122}$$

which is non symmetric. Owing to the strong coupling between the mechanical and the pore fluid problem a monolithic solution of (122) is preferred using a Newton scheme. As far as the numerical performance of the proposed implementation is concerned, it can be outlined that quadratic rate of convergence for the global Newton iteration in each step has been obtained in the computation. A typical rate is reported is Table 1.

| INCREMENT NO.: 50 | | |
|---|---|---|
| Iteration n.: 0 | Residuum Norm: | 1.53800E-03 |
| Iteration n.: 1 | Residuum Norm: | 1.18553E+01 |
| Iteration n.: 2 | Residuum Norm: | 1.40621E+01 |
| Iteration n.: 3 | Residuum Norm: | 1.23343E+00 |
| Iteration n.: 4 | Residuum Norm: | 6.19783E-02 |
| Iteration n.: 5 | Residuum Norm: | 2.09049E-05 |
| Iteration n.: 6 | Residuum Norm: | 6.28546E-09 |
| INCREMENT NO.: 75 | | |
| Iteration n.: 0 | Residuum Norm: | 1.59534E-03 |
| Iteration n.: 1 | Residuum Norm: | 9.82091E+00 |
| Iteration n.: 2 | Residuum Norm: | 1.42705E+01 |
| Iteration n.: 3 | Residuum Norm: | 1.41873E+00 |
| Iteration n.: 4 | Residuum Norm: | 6.81044E-02 |
| Iteration n.: 5 | Residuum Norm: | 2.85757E-05 |
| Iteration n.: 6 | Residuum Norm: | 8.62292E-09 |

Table 1: Rate of convergence for the implemented Newton-Rapson scheme (from the second example, using Drucker-Prager law with $\varphi = 5^0$).

## 8 Numerical Examples

It is difficult to choose appropriate tests to validate the model developed in the previous sections and its implementation in the computer code. Indeed there are no analytical solution for this type of coupled problems (to the author's knowledge), where deformations of the solid skeleton are studied with saturated-unsaturated flow of mass transfer. There are also very few documented laboratory experiments. One of these is the experiment conducted by Liakopoulos [26] on the isothermal drainage of water from a vertical column of water saturated sand (Figure 4). A column of perspex, 1 meter high, was packed by Del Monte sand and instrumented to measure the moisture tension at several points along the column. Before starting the experiment ($t < 0$) water was continuously added from the

top and was allowed to drain freely at the bottom through a filter. The flow was carefully regulated until the tensiometers read zero pore pressure. At $t = 0$ the water supply was ceased and the tensiometers reading were recorded. Only the porosity and the hydraulic properties of Del Monte sand were measured by [26] by an independent set of experiments, while the mechanical parameters are those of [27], where the Liakopoulos' test with a geometrically linear model is studied. The material parameters and the experimental constitutive laws for $S_w(p^c)$ and $k^{rw}(S_w)$ used in the computation are listed in Table 2.

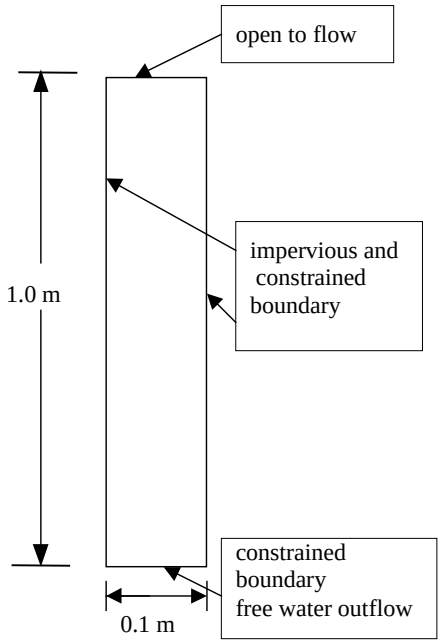


Figure 4: Scheme of the Liakopoulos' test.

| | |
|---|---|
| Porosity | $n = 0.2975$ |
| Isotropic permeability | $k = 4.3 \cdot 10^{-6} m/s$ |
| Solid grain density | $\rho^s = 2000 kg/m^3$ |
| Water density | $\rho^w = 1000 kg/m^3$ |
| Gravity acceleration | $g = 9.81 m/s^2$ |
| Water saturation | $S_w = 1.0 - 1.9722 \cdot 10^{11} p^{c2.4279}$ |
| Relative permeability for water | $k^{rw} = 1.0 - 2.207(1 - S_w)^{1.0121}$ |
| Solid bulk modulus [27] | $K = 2166.77 kN/m^2$ |
| Solid shear modulus [27] | $G = 464.29 kN/m^2$ |

Table 2: Material parameters used in the computation of the Liakopoulos' test.

The column is discretised with 10 $Q_2Q_1$ finite elements for the solid displacements and the water pressure, respectively (i.e. 9 nodes for the solid, 4 nodes for the fluid). The

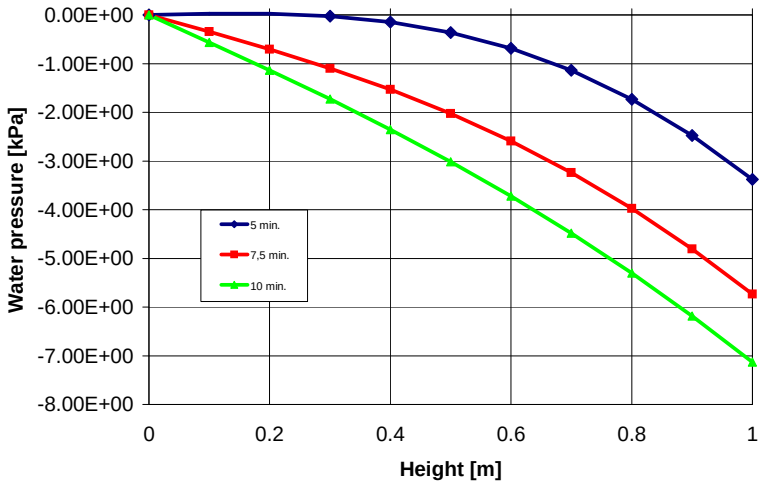


Figure 5: Water pressure vs. column height.

upper and lower boundaries are drained (water pressure is hence assumed to be at atmospheric value), while the other boundaries are impervious. Horizontal displacements are constrained on the lateral surfaces while the bottom surface is also vertically constrained. Zero initial conditions are assumed and gravity acceleration is considered during the computation, since the gravity load is the driven force of the experiment. The hyperelastic constitutive law of eq.(91) is utilized for the solid skeleton. The experiment reveals the desaturation of the column from the top to the bottom surface. This behaviour is well described from the model, as it can be observed in Figure 5, where only capillary pressures (negative water pressures) appear.

The second example deals with the analysis of a representative square domain of water saturated porous material loaded by a rigid footing (Figure 6).

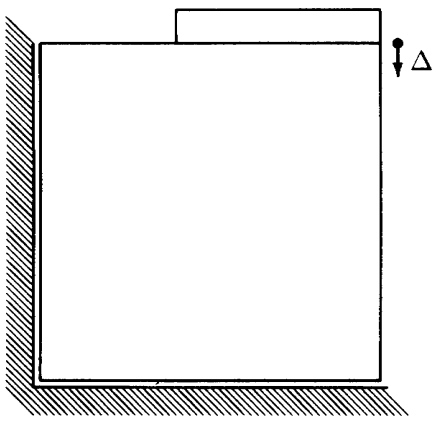


Figure 6: Rigid footing on a square domain of porous elastoplastic material.

This example was solved in [28] using the linear theory. The BVP is now solved numer-

ically using the formulation developed in the previous sections. Plain strain conditions are assumed. The homogeneous soil domain has side length of $l = 10m$, with the rigid footing spanning over $5m$ at the right part of the top surface. On the boundary, the horizontal and vertical displacements are constrained respectively on the left and bottom surface. Drainage of the water is allowed only through the unloaded part of the top surface of the domain. The solid skeleton is assumed to obey the elastoplastic von Mises or the Drucker-Prager constitutive model, both with isotropic linear softening behaviour as a phenomenological description of damage effects. The material parameters used in the computation are listed in Table 3.

| | |
|---|---|
| Solid bulk modulus | $K = 8333kN/m^2$ |
| Solid shear modulus | $G = 3486kN/m^2$ |
| initial yield stress | $y_0 = 100kN/m^2$ |
| linear softening modulus | $h = -10kN/m^2$ |
| initial apparent cohesion | $c_0 = 100kN/m^2$ |
| angle of internal friction | $\phi = 20^0$ |
| angle of dilatancy | $\varphi = -10^0, 0^0, +5^0, +10^0$ |
| isotropic permeability | $k = 0.0001m/s$ |
| Solid grain density | $\rho^s = 2000kg/m^3$ |
| Water density | $\rho^w = 1000kg/m^3$ |
| gravity acceleration | $g = 9.81m/s^2$ |
| Water saturation | $S_w = 1.0 - 1.9722 \cdot 10^{11} p^{c2.4279}$ |
| Relative permeability for water | $k^{rw} = 1.0 - 2.207(1 - S_w)^{1.0121}$ |

Table 3: Material parameters used in the computation of the localisation example.

The von Mises law has been selected as a reference material law used to test the implementation and to describe qualitatively the mechanical behaviour of clays under undrained conditions, while the Drucker-Prager law has been chosen to simulate the behaviour of dilatant/contractant geomaterials such as dense and loose sands, respectively. The loading is applied quasi-statically to the rigid footing by displacement control with a constant vertical velocity of $5e-3m/s$ until the maximum displacement is obtained. The domain has been discretised using 20 x 20 $S_2Q_1$ elements for the solid and the fluid mesh (i.e. 8 nodes for the solid, 4 nodes for the fluid).

Figure 7 shows the distribution of the equivalent plastic strain at the end of the load history ($0.5m$ in this case) on the deformed configuration using the von Mises material model. No magnification of the displacements has been used in this and all the following figures. The plastic zone indicates the pronounced accumulation of inelastic strains in a narrow band, while the deformed configuration outlines the classical slip of a part of the domain on the other. Figure 8 shows the excess water pressures at the end of the load history (values expressed in $kPa$), where only positive pressure values can be observed due to the compressive load in a solid skeleton with isochoric plastic flow.

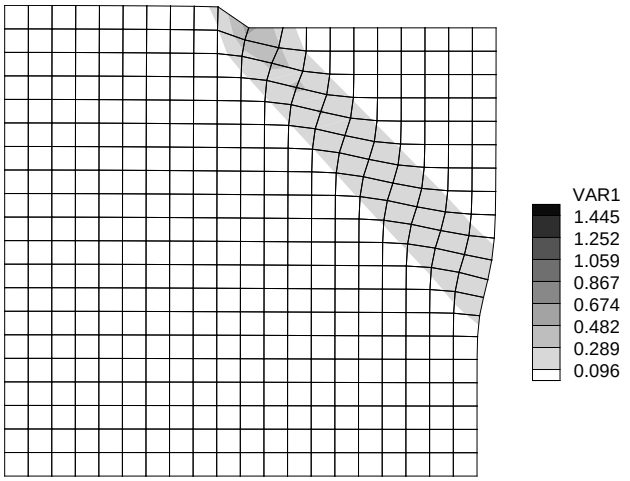


Figure 7: Equivalent plastic strain contour using von Mises law.

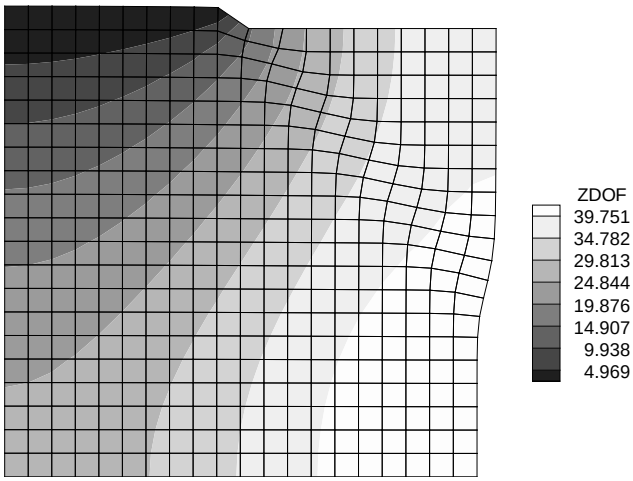


Figure 8: Excess water pressure contour using von Mises law (kPa).

The effect of the plastic dilatancy/contractancy is shown by analysing the square panel using the Drucker-Prager material law. The sample has been solved using different values of the angle of dilatancy: $0^0, +5^0, +10^0$ and $-10^0$. In particular, Figures 9 and 10 show the equivalent plastic strain and the excess water pressure distribution at the end of the load history in case of zero dilatancy (which means isochoric plastic flow). The resulting shear band and the deformation pattern are hence very similar to those obtained using the von Mises material law, as it can be observed by comparison with Figures 7 and 8. Increasing the value of the angle of dilatancy ($\varphi = 5^0$ and $10^0$, see Figures 11 and 12, respectively), an increase of the horizontal displacement of the right side of the panel, due to the increase of volumetric plastic strain with dilatancy, can be observed. The opposite behaviour appears in case of negative value of the dilatancy angle, see Figure 13, where the equivalent plastic strain contour in case of dilatancy angle of $-10^0$ is depicted.

The effect of the plastic dilatancy/contractany is evidenced also in the contour of the water pressures. In fact the variation of the porosity with the deformation of the medium, see eq.(49) and the localisation of the dilatant plastic strains imply the presence of negative water pressure, with the lowest values inside the plastic zones (Figures 14 and 15), as opposed to the case of contractant plastic flow (Figure 16). The presence of negative pressures is not surprising. In fact, it was experimentally observed at localisation by [1] and [2] during biaxial tests of globally undrained dense sands under imposed displacements. In particular, the value of $-80$ and $-91kPa$ was measured by the two authors, respectively. At those pressures, partially saturated condition due to cavitation of the pore water was observed, which means the presence of the vapour phase separated from the liquid phase by a meniscus. The values of negative water pressures below the cavitation pressure computed in the numerical example of Figure 15 suggest the presence of cavitation phenomenon inside shear band and close to it.
The dilatant behaviour of the used constitutive model for the solid skeleton is shown also in Figure 17 where the contour of the porosity for the case of Drucker-Prager with dilatant angle of $10^0$ and friction angle of $20^0$ is depicted. It can be observed that the porosity increase only inside the shear band, while decrease outside it (the initial value at $t = 0$ was 0.3). Figure 18 shows the contour of the water saturation for the same example, where in particular it can be observed the desaturation of the zones occupied by the shear band and of that close to it.
The effect of the plastic dilatancy/contractany is evidenced also in Figures 19 and 20, where water velocity in case of dilatant and contractant material is shown. Different directions of the fluid can be noted, flowing into the band in case of dilatant material, out of it in the other case.

**Remarks**: negative water pressures start from the top surface, close to the left corner of the foundation, where the dilatant shear band first appears, and propagate inside the plastic zone following the evolution of the shear band. Then, they propagate also outside the band due to the filtration process generated by the high pressure gradient in conjunction with the quasi-static process, until they occupy almost all the domain, as it

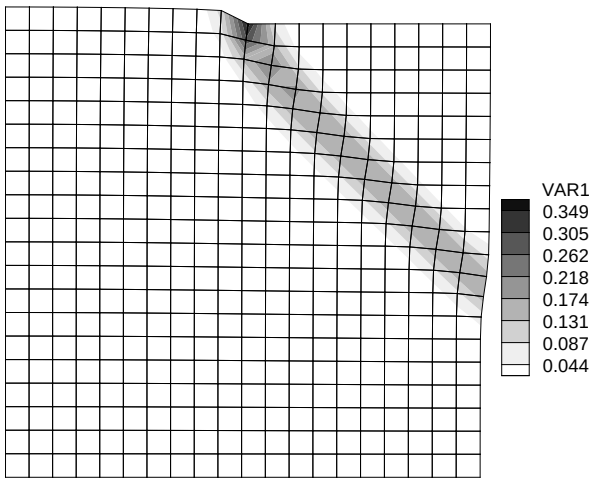


Figure 9: Equivalent plastic strain contour using Drucker-Prager law with $\varphi = 0^0$.

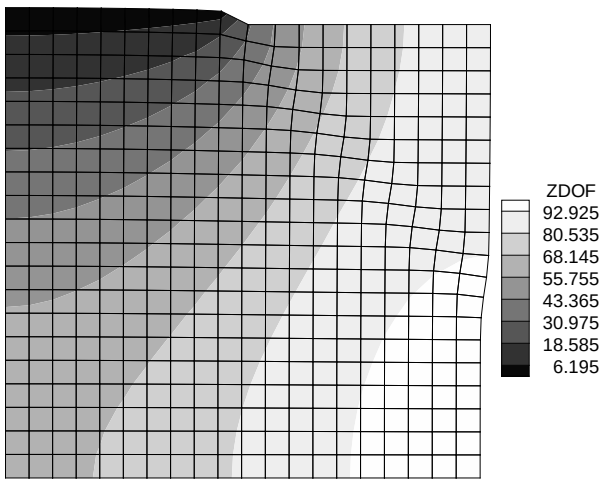


Figure 10: Excess water pressure contour using Drucker-Prager law with $\varphi = 0^0$ (kPa).

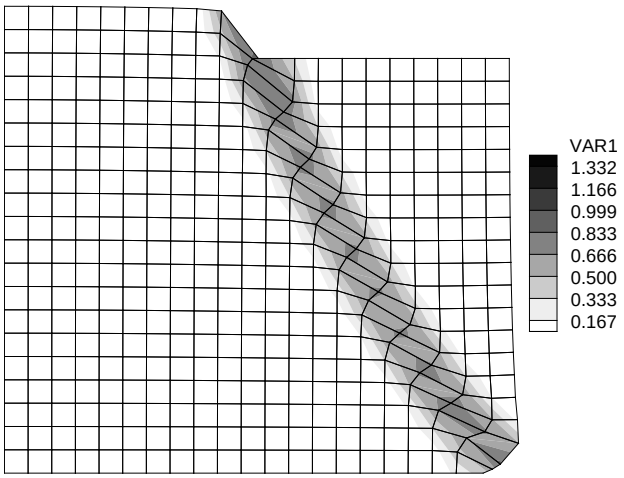


Figure 11: Equivalent plastic strain contour using Drucker-Prager law with $\varphi = 5^0$.

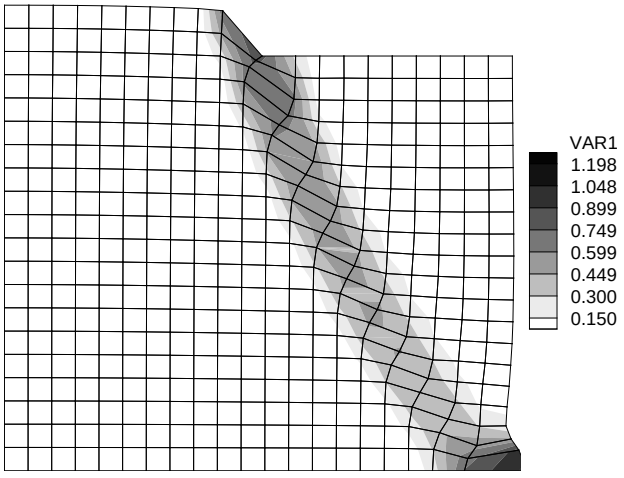


Figure 12: Equivalent plastic strain contour using Drucker-Prager law with $\varphi = 10^0$.

can be observed in Figure 15. This phenomenon is dependent on the value of the time step: decreasing its value, a reduced zone with negative water pressure has been observed, but it is always present. The localisation of the negative pressures could be probably easily captured in the dynamic case, as shown in ([7], [29], [30]) using a geometrically linear model.

## Conclusions

This paper shows a mathematical model and the related finite element discretisation of quasi-static and isothermal inelastic saturated and partially geomaterials, assuming incompressible constituents at microscopic level. The governing equations are derived in material and spatial formulation. The elasto-plastic behaviour of the solid skeleton is based on the multiplicative decomposition of the deformation gradient in an elastic and plastic part and is developed in spatial setting. The solid effective stress is hyperelastic or limited by the von Mises or the Drucker-Prager yield criterion with isotropic linear softening. A particular apex formulation is developed for the later case. The water behaves following Darcy's law. Consistent linearisation of the non-linear equation system and finite element formulation are derived. Numerical results of this research in progress on large elastic or inelastic strains in saturated and partially saturated porous media are shown.

## Acknowledgements

The author wish to thank Prof. B.A. Schrefler (University of Padua, Italy) and Prof. P. Steinmann (University of Kaiserslautern, Germany) for their useful discussions, providing the much appreciated motivation and inspirational support, and the *Programma Vigoni 2000* from CRUI, Italy, for the financial support of his stay at the University of Kaiserslautern.

## References

[1] Mokni, M., Desrues, J., Strain Localisation Measurements in Undrained Plane-strain Biaxial Tests on Hostun RF Sand, *Mech. Cohes-Frict. Mater.* 4, 419-441, 1998.

[2] Vardoulakis, J., Sulem J., *Bifurcation Analysis in Geomechanics*, Blakie Academic and Professional, 1995, London.

[3] Peters, J.F., Lade, P.V., Bro, A., Shear Band Formation in Triaxial and Plane Strain tests, Advanced Triaxial Testing of Soil and Rock, ASTM STP 977, Donaghe R.T., Chaney R.C. and Silver M.L. eds., *Am. Soc. Testing and Materials*, Philadelphia, 604, 1988.

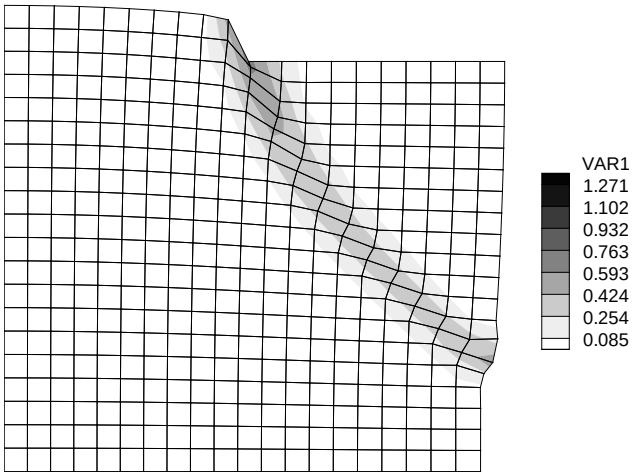


Figure 13: Equivalent plastic strain contour using Drucker-Prager law with $\varphi = -10^0$.

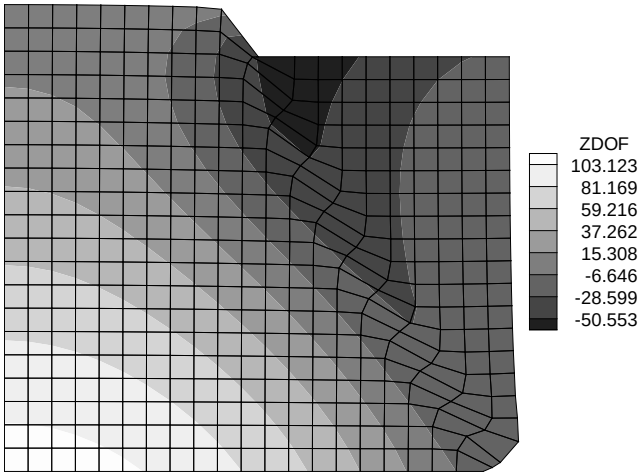


Figure 14: Water pressure contour using Drucker-Prager law with $\varphi = 5^0$ (kPa).

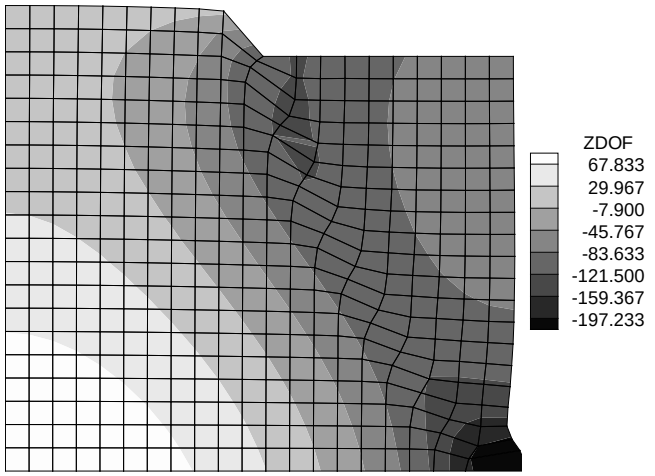


Figure 15: Water pressure contour using Drucker-Prager law with $\varphi = 10^0$ (kPa).

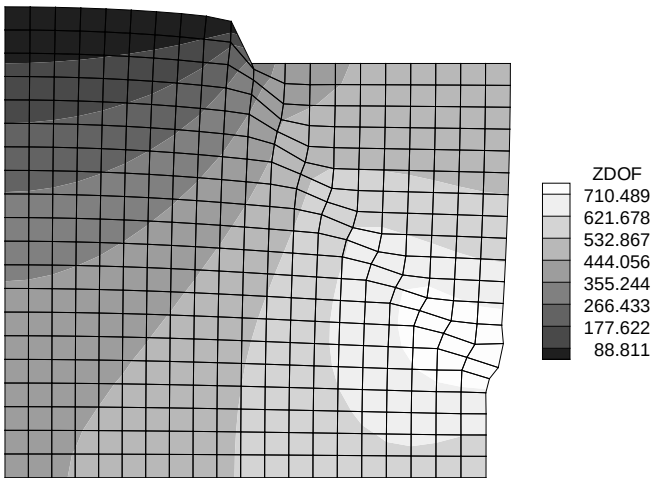


Figure 16: Excess water pressure contour using Drucker-Prager law with $\varphi = -10^0$ (kPa)
.

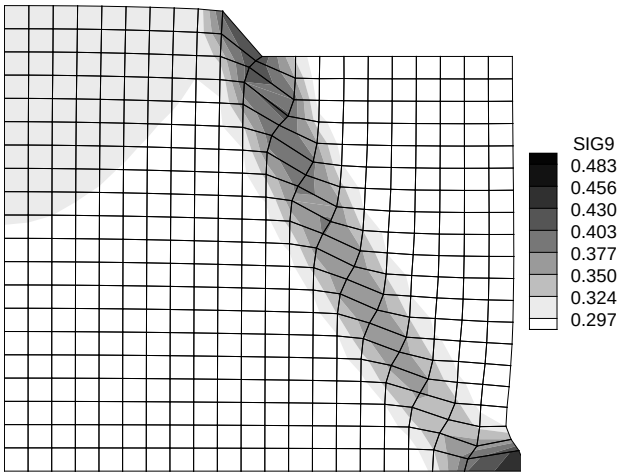


Figure 17: Porosity contour using Drucker-Prager law with $\varphi = 10^0$.

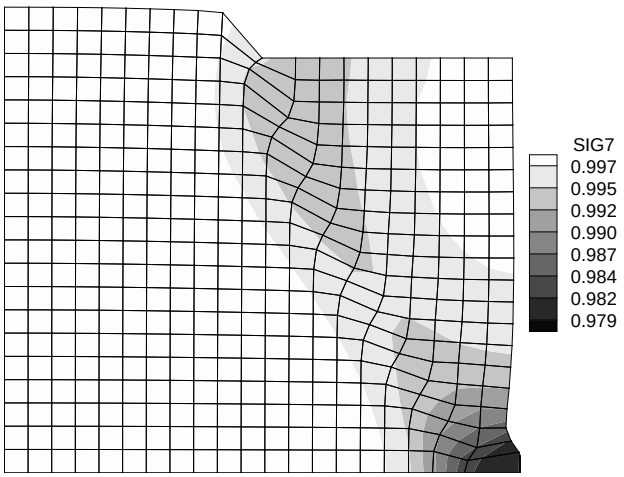


Figure 18: Water saturation contour using Drucker-Prager law with $\varphi = 10^0$.

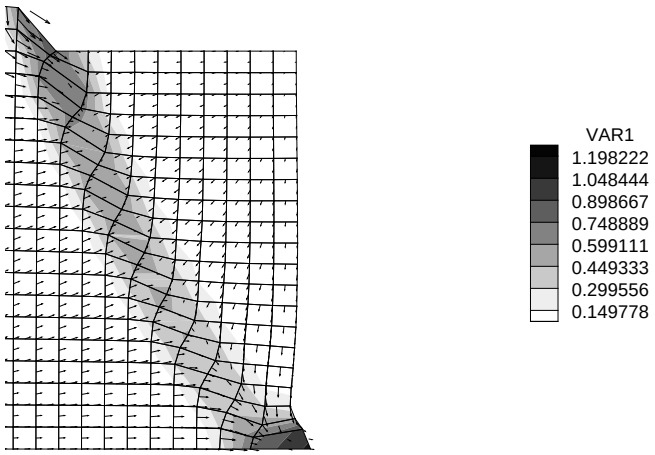


Figure 19: Water velocity close the shear band using Drucker-Prager law with $\varphi = 10^0$.

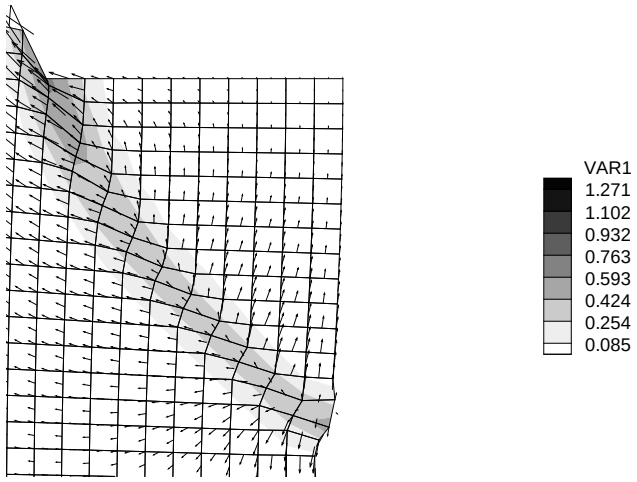


Figure 20: Water velocity close the shear band using Drucker-Prager law with $\varphi = -10^0$.

[4] Meroi, E., Schrefler B.A., Zienkiewicz O.C., Large Strain Static and Dynamic Semi-Saturated Soil Behaviour, *Int. J. Num. Analytical Methods Geomech.* 19, 2, 81-106, 1995.

[5] Sanavia, L., Schrefler, B.A., Stein, E., Steinmann, P., Modelling of localisation at finite inelastic strain in fluid saturated porous media, *Proc. IUTAM Symposium on Theoretical and Numerical Methods in Continuum Mechanics of Porous Materials*, W. Ehlers eds., Kluwer Academic Publishers, 239-244, 2001.

[6] Lewis, R.W., Schrefler, B.A., *The Finite Element Method in the Static and Dynamic Deformation and Consolidation of Porous Media*, John Wiley, New York, 1998.

[7] Schrefler, B.A., Sanavia, L., Majorana, C.E., A Multiphase Medium Model for Localisation and Postlocalisation Simulation in Geomaterials, *Mechanics of Cohesive-frictional materials* 1, 95-114, 1996.

[8] Zhang H.W., Sanavia L., Schrefler B.A., An Internal length Scale in Strain Localisation of Multiphase Porous Media, *Mech. Cohes.-Frict. Mater.*4, 433-460, 1999.

[9] Hassanizadeh, M., Gray, W.G., General Conservation Equations for Multi-phase System: 1. Averaging technique, *Adv. Water Res.* 2, 131-144, 1979, General Conservation Equations for Multi-Phase System: 2. Mass, Momenta, Energy and Entropy Equations, *Adv. Water Res.* 2, 191-201, 1979.

[10] Hassanizadeh, M., Gray, W.G., General Conservation Equations for Multi-Phase System: 3. Constitutive Theory for Porous Media Flow, *Adv. Water Res.* 3, 25-40, 1980.

[11] de Boer, R., *Theory of Porous Media: Highlightin Historical Development and Current State*, Springer, 2000.

[12] Gray, W.G., Hassanizadeh, M., Unsaturated Flow Theory including Interfacial Phenomena, *Water Resources Res.* 27, (8), 1855-1863, 1991.

[13] Zienkiewicz, O.C., Chan, A., Pastor, M., Schrefler, B.A., Shiomi T., *Computational Geomechanics with special Reference to Earthquake Engineering*, Wiley Chichester, 1999.

[14] Marsden, J.E., Hughes, T.J.R., *Mathematical Foundations of Elasticity*, Prentice-Hall Inc., 1983.

[15] Lee, E.H., Elastic-Plastic Deformation at Finite Strains, *J. Appl. Mech.*, 1-6, 1969.

[16] Nemat-Nasser, S., On Finite Plastic Flow of Crystalline Solids and Geomaterials, *Transactions of ASME*, 50, 1114-1126, 1983.

[17] Simo, J.C. *Numerical Analysis and Simulation of Plasticity*, In P.G. Ciarlet and J.L. Lions, editors, Numerical Methods for Solids (Part 3), vol. 6 of Handbook of Numerical Analysis. North-Holland, 1998.

[18] Drucker, D.C., Prager, W., Soil Mechanics and Plastic Analysis or Limit Design, *Quart. Appl. Math.* 10, 2, 157-165, 1952.

[19] Simo, J.C., Hughes, T.J.R., *Computational Inelasticity*, Springer, 1998.

[20] Ciarlet P.G., *Mathematical Elasticity. Volume I: Three-Dimensional Elasticity*, Elsevier Science, 1988.

[21] Reese S., Elastopastic Material Behaviour with Large Elastic and Large Plastic Deformation, *ZAMM Z. Angew. Math. Mech.*, 77, S277-S278, 1997.

[22] Wriggers, P., *Continuum Mechanics, Non-linear Finite Element Techniques and Computational Stability*, Progress in computational Analysis of Inelastic Structures, CISM n. 321, eds. Stein E., Springer-Verlag Wien, New York, 1993.

[23] Simo J.C., Taylor R., Consistent Tangent Operators for Rate-Independent Elastoplasticity, *Comp. Meth. In Applied Mech. Eng.* 48, 101-118, 1985.

[24] Miehe, C., Computation of Isotropic Tensor Functions, *Comm. Num. Meth. Eng.* 9, 889-896, 1993.

[25] Hofstetter G., Taylor R.L., Non-associative Drucker-Prager plasticity at finite srains, *Comm. Appl. Num. Meth. Engrg.* 6, 583-589, 1990.

[26] Liakopoulos, A.C., *Transient flow through unsaturated porous media*, PhD. Thesis, University of California-Berkeley, 1965.

[27] Schrefler, B.A., Simoni, L., A unified approach to the analysis of saturated-unsaturated elastoplastic porous media, *Proc. Numerical Methods in Geomechanics*, Balkema, 1988.

[28] Steinmann, P., A finite element formulation for Strong Discontinuities in Fluid-Saturated Porous Media, *Mech. Cohes.-Frict. Mater.* 4, 133-152, 1999.

[29] Gawin, D., Sanavia, L., Scherfler, B.A., Cavitation Modelling in Saturated Geomaterials with Application to Dynamic Strain Localisation, *Int. J. Num. Methods in Fluids* 27, 109-125,1998.

[30] Zhang, H.,W., Sanavia, L., and Schrefler, B.A., Numerical analysis of dynamic strain localisation in initially water saturated dense sand with a modified generalised plasticity model, *Comp. and Struct.* 79, 441-459, 2001.